Editors' Suggestion

Measurement of $\cos 2\beta$ in $B^0 \to D^{(*)}h^0$ with $D \to K^0_S\pi^+\pi^-$ decays by a combined time-dependent Dalitz plot analysis of *BABAR* and Belle data

I. Adachi,[31,28,B] T. Adye,[106,A] H. Ahmed,[114,A] J. K. Ahn,[53,B] H. Aihara,[130,B] S. Akar,[97,A] M. S. Alam,[116,A] J. Albert,[136b,A] F. Anulli,[104a,A] N. Arnaud,[53,A] D. M. Asner,[10,B] D. Aston,[111,A] H. Atmacan,[112,B] T. Aushev,[76,B] R. Ayad,[119,B] I. Badhrees,[119,50,B] A. M. Bakich,[118,B] Sw. Banerjee,[64,A] V. Bansal,[94,B] R. J. Barlow,[68,*,A] G. Batignani,[100a,100b,A] A. Beaulieu,[136b,A] P. Behera,[39,B] M. Bellis,[105,A] E. Ben-Haim,[97,A] D. Bernard,[59,A] F. U. Bernlochner,[136b,A] S. Bettarini,[100a,100b,A] D. Bettoni,[24a,A] A. J. Bevan,[62,A] V. Bhardwaj,[35,B] B. Bhuyan,[37,A] F. Bianchi,[133a,133b,A] M. Biasini,[99a,99b,A] J. Biswal,[46,B] V. E. Blinov,[11,12,13,A] M. Bomben,[97,A] A. Bondar,[11,12,B] G. R. Bonneaud,[97,A] A. Bozek,[88,B] C. Bozzi,[24a,A] M. Bračko,[69,46,B] T. E. Browder,[30,B] D. N. Brown,[7,A] D. N. Brown,[64,A] C. Bünger,[105,A] P. R. Burchat,[105,A] A. R. Buzykaev,[11,A] R. Calabrese,[24a,24b,A] A. Calcaterra,[25,A] G. Calderini,[97,A] S. Di Carlo,[55,B] M. Carpinelli,[100a,100b,†,A] C. Cartaro,[111,A] G. Casarosa,[100a,100b,A] R. Cenci,[70,A] D. S. Chao,[17,A] J. Chauveau,[97,A] R. Cheaib,[76,A] A. Chen,[84,B] C. Chen,[44,A] C. H. Cheng,[17,A] B. G. Cheon,[29,B] K. Chilikin,[58,B] K. Cho,[52,B] Y. Choi,[117,B] S. Choudhury,[38,B] M. Chrzaszcz,[100a,A] G. Cibinetto,[24a,24b,A] D. Cinabro,[139,B] J. Cochran,[44,A] J. P. Coleman,[60,A] M. R. Convery,[111,A] G. Cowan,[63,A] R. Cowan,[71,A] L. Cremaldi,[76,A] S. Cunliffe,[22,B] N. Dash,[36,B] M. Davier,[55,A] C. L. Davis,[64,A] F. De Mori,[133a,133b,A] G. De Nardo,[82a,82b,A] A. G. Denig,[67,A] R. de Sangro,[25,A] B. Dey,[75a,A] F. Di Lodovico,[62,A] S. Dittrich,[105,A] Z. Doležal,[17,B] J. Dorfan,[111,A] Z. Drásal,[17,B] V. P. Druzhinin,[11,12,A] W. Dunwoodie,[111,A] M. Ebert,[111,A] B. Echenard,[17,A] S. Eidelman,[11,12,B] G. Eigen,[6,A] A. M. Eisner,[16,A] S. Emery,[107,A] D. Epifanov,[11,12,B] J. A. Ernst,[116,A] R. Faccini,[104a,104b,A] J. E. Fast,[94,B] M. Feindt,[48,B] F. Ferrarotto,[104a,A] F. Ferroni,[104a,104b,A] R. C. Field,[111,A] A. Filippi,[133a,A] G. Finocchiaro,[25,A] E. Fioravanti,[24a,24b,A] K. T. Flood,[17,A] F. Forti,[100a,100b,A] M. Fritsch,[8,A] B. G. Fulsom,AB[111,94] E. Gabathuler,[60,‡,A] D. Gamba,[133b,133b,A] R. Garg,[96,B] A. Garmash,[11,12,B] J. W. Gary,[15,A] I. Garzia,[24a,24b,A] V. Gaur,[137,B] A. Gaz,[95a,A] M. Gelb,[48,B] T. J. Gershon,[138,A] L. Li Gioi,[72,B] M. A. Giorgi,[100a,100b,A] A. Giri,[38,B] R. Godang,[76,§,A] P. Goldenzweig,[48,B] B. Golob,[61,46,B] V. B. Golubev,[11,12,A] R. Gorodeisky,[123,A] W. Gradl,[67,A] M. T. Graham,[111,A] E. Grauges,[2,A] K. Griessinger,[67,A] A. V. Gritsan,[47,A] O. Grünberg,[105,A] E. Guido,[133a,B] N. Guttman,[123,A] A. Hafner,[67,A] T. Hara,[31,28,B] P. F. Harrison,[138,A] C. Hast,[111,A] K. Hayasaka,[90,B] C. Hearty,[9a,9b,A] M. Heck,[48,B] M. T. Hedges,[30,B] M. Heß,[105,A] S. Hirose,[81,B] D. G. Hitlin,[17,A] K. Honscheid,[92,A] W.-S. Hou,[87,B] Z. Huard,[20,A] C. Van Hulse,[4,B] D. E. Hutchcroft,[60,A] K. Inami,[81,B] G. Inguglia,[22,B] W. R. Innes,[111,‡,A] A. Ishikawa,[128,B] R. Itoh,[31,28,B] M. Iwasaki,[93] Y. Iwasaki,[31,B] J. M. Izen,[126,A] W. W. Jacobs,[40,B] A. Jawahery,[70,A] C. P. Jessop,[91,A] S. Jia,[5,B] Y. Jin,[130,B] K. K. Joo,[19,B] T. Julius,[74,B] A. B. Kaliyar,[39,B] K. H. Kang,[54,B] G. Karyan,[22,B] R. Kass,[92,A] H. Kichimi,[31,B] D. Y. Kim,[110,B] J. B. Kim,[53,B] K. T. Kim,[55,B] S. H. Kim,[29,B] J. Kim,[17,A] P. Kim,[111,A] G. J. King,[136b,A] K. Kinoshita,[20,B] H. Koch,[8,A] P. Kodyš,[18,B] Yu. G. Kolomensky,[7,A] S. Korpar,[69,46,B] D. Kotchetkov,[30,B] R. Kowalewski,[136b,A] E. A. Kravchenko,[11,12,A] P. Križan,[61,46,B] R. Kroeger,[76,B] P. Krokovny,[11,12,B] T. Kuhr,[65,B] R. Kulasiri,[49,B] A. Kuzmin,[11,12,B] Y.-J. Kwon,[142,B] H. M. Lacker,[33,A] G. D. Lafferty,[68,A] L. Lanceri,[134,A] J. S. Lange,[27,B] D. J. Lange,[57,A] A. J. Lankford,[14,A] T. E. Latham,[138,A] T. Leddig,[105,A] F. Le Diberder,[55,A] I. S. Lee,[29,B] S. C. Lee,[54,B] J. P. Lees,[1,A] D. W. G. S. Leith,[111,A] L. K. Li,[41,B] Y. B. Li,[98,B] Y. Li,[17,A] J. Libby,[39,B] D. Liventsev,[137,31,B] W. S. Lockman,[16,A] O. Long,[15,A] J. M. LoSecco,[91,A] X. C. Lou,[126,A] M. Lubej,[46,B] T. Lueck,[136b,A] S. Luitz,[111,A] T. Luo,[23,B] E. Luppi,[24a,24b,A] A. Lusiani,[100a,100c,A] A. M. Lutz,[55,A] D. B. MacFarlane,[111,A] J. MacNaughton,[31,B] U. Mallik,[43,A] E. Manoni,[99a,A] G. Marchiori,[97,A] M. Margoni,[95a 95b,A] S. Martellotti,[25,A] F. Martinez-Vidal,[135,A] M. Masuda,[129,B] T. Matsuda,[77,B] T. S. Mattison,[9b,A] D. Matvienko,[11,12,B] J. A. McKenna,[9b,A] B. T. Meadows,[20,A] M. Merola,[82a,82b,B] K. Miyabayashi,[83,B] T. S. Miyashita,[17,A] H. Miyata,[90,B] R. Mizuk,[58,79,80,B] G. B. Mohanty,[120,B] T. Mori,[81,B] D. R. Muller,[111,A] T. Müller,[48,B] R. Mussa,[133a,B] E. Nakano,[93,B] M. Nakao,[31,28,B] T. Nanut,[46,B] K. J. Nath,[37,B] M. Nayak,[139,31,B] H. Neal,[111,A] N. Neri,[75a,A] N. K. Nisar,[101,B] S. Nishida,[31,28,B] I. M. Nugent,[136b,A] B. Oberhof,[100a,100b,A] J. Ocariz,[97,A] S. Ogawa,[127,B] P. Ongmongkolkul,[17,A] H. Ono,[89,90,B] A. P. Onuchin,[11,12,13,A] A. Oyanguren,[135,A] P. Pakhlov,[58,79,B] G. Pakhlova,[58,80,B] B. Pal,[20,B] A. Palano,[3,A] F. Palombo,[75a,75b,A] W. Panduro Vazquez,B[16] E. Paoloni,[100a,100b,A] S. Pardi,[82a,B] H. Park,[54,B] S. Passaggio,[26,A] C. Patrignani,[26,¶,A] P. Patteri,[25,A] S. Paul,[121,B] I. Pavelkin,[80,B] D. J. Payne,[60,A] T. K. Pedlar,[66,B] D. R. Peimer,[123,A] I. M. Peruzzi,[25,A] M. Piccolo,[25,A] L. E. Piilonen,[137,B] A. Pilloni,[104a,104b,A] G. Piredda,[104a,†,A] V. Poireau,[1,A] F. C. Porter,[17,A] M. Posocco,[95a,A] S. Prell,[44,A] R. Prepost,[140,A] E. M. T. Puccio,[115,A] M. V. Purohit,[112,A] B. G. Pushpawela,[20,A] M. Rama,[100a,A] A. Randle-Conde,[113,A] B. N. Ratcliff,[111,A] G. Raven,[86,A] P. K. Resmi,[39,B] J. L. Ritchie,[125,A] M. Ritter,[65,B] G. Rizzo,[100a,100b,A] D. A. Roberts,[70,A] S. H. Robertson,[73a,73b,A] M. Röhrken,AB[17,48,**] J. M. Roney,[136b,A] A. Roodman,[111,A] A. Rossi,[99a,A] M. Rotondo,[25,A] M. Rozanska,[88,B] G. Russo,[82a,B] R. Sacco,[62,A] S. Al Said,[119,51,B] Y. Sakai,[31,28,B] S. Sandilya,[20,B] L. Santelj,[31,B] V. Santoro,[24a,A] T. Sanuki,[128,B] V. Savinov,[101,B] O. Schneider,[56,B] G. Schnell,[4,34,B] T. Schroeder,[8,A] K. R. Schubert,[67,A] C. Schwanda,[42,B] A. J. Schwartz,[20,B] R. F. Schwitters,[125,A] C. Sciacca,[82a,82b,A] R. M. Seddon,[73b,A] Y. Seino,[90,B] S. J. Sekula,[113,A] K. Senyo,[141,B] O. Seon,[81,B] S. I. Serednyakov,[11,12,A] M. E. Sevior,[74,B] V. Shebalin,[11,12,B] T.-A. Shibata,[131,B]

N. Shimizu,[130,B] J.-G. Shiu,[87,B] G. Simi,[95a,95b,A] F. Simon,[72,122,B] F. Simonetto,[95a,95b,A] Yu. I. Skovpen,[11,12] J. G. Smith,[21,A] A. J. S. Smith,[102,A] R. Y. So,[9b,A] R. J. Sobie,[136a,136b,A] A. Soffer,[123,A] M. D. Sokoloff,[20,A] E. P. Solodov,[11,12,A] E. Solovieva,[58,80,B] S. M. Spanier,[124,A] M. Starič,[46,B] R. Stroili,[95a,95b,A] M. K. Sullivan,[111,A] K. Sumisawa,[31,28,B] T. Sumiyoshi,[132,B] D. J. Summers,[76,A] L. Sun,[20,††,A] M. Takizawa,[109,32,103,B] U. Tamponi,[133a,B] K. Tanida,[45,B] P. Taras,[78,A] N. Tasneem,[136b,A] F. Tenchini,[74,B] V. Tisserand,[1,A] K. Yu. Todyshevx,[11,12] C. Touramanis,[60,A] M. Uchida,[131,B] T. Uglov,[58,80,B] Y. Unno,[29,B] S. Uno,[31,28,B] S. E. Vahsen,[30,B] G. Varner,[30,B] G. Vasseur,[107,A] J. Va'vra,[111,A] D. Červenkov,[18,B] M. Verderi,[59,A] L. Vitale,[134,A] V. Vorobyev,[11,12,B] C. Voß,[105,A] S. R. Wagner,[21,A] E. Waheed,[74,B] R. Waldi,[105,A] J. J. Walsh,[100a,A] B. Wang,[20,B] C. H. Wang,[85,B] M.-Z. Wang,[87,B] P. Wang,[41,B] F. F. Wilson,[106,A] J. R. Wilson,[112,A] W. J. Wisniewski,[111,A] E. Won,[53,B] G. Wormser,[55,A] D. M. Wright,[57,A] S. L. Wu,[140,A] C. Z. Yuan,[41,B] Y. Yusa,[90,B] S. Zakharov,[58,80,B] A. Zallo,[25,A] L. Zani,[100a,100b,A] Z. P. Zhang,[108,B] V. Zhilich,[11,12,B] V. Zhukova,[58,79,B] V. Zhulanov,[11,12,B] and A. Zupanc[61,46,B]

(*BABAR* Collaboration)[A]
(Belle Collaboration)[B]

[1]*Laboratoire d'Annecy-le-Vieux de Physique des Particules (LAPP), Université de Savoie, CNRS/IN2P3, F-74941 Annecy-Le-Vieux, France*
[2]*Universitat de Barcelona, Facultat de Fisica, Departament ECM, E-08028 Barcelona, Spain*
[3]*INFN Sezione di Bari and Dipartimento di Fisica, Università di Bari, I-70126 Bari, Italy*
[4]*University of the Basque Country UPV/EHU, 48080 Bilbao, Spain*
[5]*Beihang University, Beijing 100191, China*
[6]*University of Bergen, Institute of Physics, N-5007 Bergen, Norway*
[7]*Lawrence Berkeley National Laboratory and University of California, Berkeley, California 94720, USA*
[8]*Ruhr Universität Bochum, Institut für Experimentalphysik 1, D-44780 Bochum, Germany*
[9a]*Institute of Particle Physics, Vancouver, British Columbia, Canada V6T 1Z1*
[9b]*University of British Columbia, Vancouver, British Columbia, Canada V6T 1Z1*
[10]*Brookhaven National Laboratory, Upton, New York 11973, USA*
[11]*Budker Institute of Nuclear Physics SB RAS, Novosibirsk 630090, Russian Federation*
[12]*Novosibirsk State University, Novosibirsk 630090, Russian Federation*
[13]*Novosibirsk State Technical University, Novosibirsk 630092, Russian Federation*
[14]*University of California at Irvine, Irvine, California 92697, USA*
[15]*University of California at Riverside, Riverside, California 92521, USA*
[16]*University of California at Santa Cruz, Institute for Particle Physics, Santa Cruz, California 95064, USA*
[17]*California Institute of Technology, Pasadena, California 91125, USA*
[18]*Faculty of Mathematics and Physics, Charles University, 121 16 Prague, Czech Republic*
[19]*Chonnam National University, Kwangju 660-701, South Korea*
[20]*University of Cincinnati, Cincinnati, Ohio 45221, USA*
[21]*University of Colorado, Boulder, Colorado 80309, USA*
[22]*Deutsches Elektronen-Synchrotron, 22607 Hamburg, Germany*
[23]*Key Laboratory of Nuclear Physics and Ion-Beam Application (MOE) and Institute of Modern Physics, Fudan University, Shanghai 200443, China*
[24a]*INFN Sezione di Ferrara, I-44122 Ferrara, Italy*
[24b]*Dipartimento di Fisica e Scienze della Terra, Università di Ferrara, I-44122 Ferrara, Italy*
[25]*INFN Laboratori Nazionali di Frascati, I-00044 Frascati, Italy*
[26]*INFN Sezione di Genova, I-16146 Genova, Italy*
[27]*Justus-Liebig-Universität Gießen, 35392 Gießen, Germany*
[28]*SOKENDAI (The Graduate University for Advanced Studies), Hayama 240-0193, Japan*
[29]*Hanyang University, Seoul 133-791, South Korea*
[30]*University of Hawaii, Honolulu, Hawaii 96822, USA*
[31]*High Energy Accelerator Research Organization (KEK), Tsukuba 305-0801, Japan*
[32]*J-PARC Branch, KEK Theory Center, High Energy Accelerator Research Organization (KEK), Tsukuba 305-0801, Japan*
[33]*Humboldt-Universität zu Berlin, Institut für Physik, D-12489 Berlin, Germany*
[34]*IKERBASQUE, Basque Foundation for Science, 48013 Bilbao, Spain*
[35]*Indian Institute of Science Education and Research Mohali, SAS Nagar, 140306, India*
[36]*Indian Institute of Technology Bhubaneswar, Satya Nagar 751007, India*
[37]*Indian Institute of Technology Guwahati, Assam 781039, India*
[38]*Indian Institute of Technology Hyderabad, Telangana 502285, India*

[39]Indian Institute of Technology Madras, Chennai 600036, India
[40]Indiana University, Bloomington, Indiana 47408, USA
[41]Institute of High Energy Physics, Chinese Academy of Sciences, Beijing 100049, China
[42]Institute of High Energy Physics, Vienna 1050, Austria
[43]University of Iowa, Iowa City, Iowa 52242, USA
[44]Iowa State University, Ames, Iowa 50011, USA
[45]Advanced Science Research Center, Japan Atomic Energy Agency, Naka 319-1195, Japan
[46]J. Stefan Institute, 1000 Ljubljana, Slovenia
[47]Johns Hopkins University, Baltimore, Maryland 21218, USA
[48]Institut für Experimentelle Teilchenphysik,
Karlsruher Institut für Technologie, 76131 Karlsruhe, Germany
[49]Kennesaw State University, Kennesaw, Georgia 30144, USA
[50]King Abdulaziz City for Science and Technology, Riyadh 11442, Kingdom of Saudi Arabia
[51]Department of Physics, Faculty of Science, King Abdulaziz University,
Jeddah 21589, Kingdom of Saudi Arabia
[52]Korea Institute of Science and Technology Information, Daejeon 305-806, South Korea
[53]Korea University, Seoul 136-713, South Korea
[54]Kyungpook National University, Daegu 702-701, South Korea
[55]Laboratoire de l'Accélérateur Linéaire, IN2P3/CNRS et Université Paris-Sud 11,
Centre Scientifique d'Orsay, F-91898 Orsay Cedex, France
[56]École Polytechnique Fédérale de Lausanne (EPFL), Lausanne 1015, Switzerland
[57]Lawrence Livermore National Laboratory, Livermore, California 94550, USA
[58]P.N. Lebedev Physical Institute of the Russian Academy of Sciences,
Moscow 119991, Russian Federation
[59]Laboratoire Leprince-Ringuet, Ecole Polytechnique, CNRS/IN2P3, F-91128 Palaiseau, France
[60]University of Liverpool, Liverpool L69 7ZE, United Kingdom
[61]Faculty of Mathematics and Physics, University of Ljubljana, 1000 Ljubljana, Slovenia
[62]Queen Mary, University of London, London, E1 4NS, United Kingdom
[63]University of London, Royal Holloway and Bedford New College,
Egham, Surrey TW20 0EX, United Kingdom
[64]University of Louisville, Louisville, Kentucky 40292, USA
[65]Ludwig Maximilians University, 80539 Munich, Germany
[66]Luther College, Decorah, Iowa 52101, USA
[67]Johannes Gutenberg-Universität Mainz, Institut für Kernphysik, D-55099 Mainz, Germany
[68]University of Manchester, Manchester M13 9PL, United Kingdom
[69]University of Maribor, 2000 Maribor, Slovenia
[70]University of Maryland, College Park, Maryland 20742, USA
[71]Massachusetts Institute of Technology, Laboratory for Nuclear Science,
Cambridge, Massachusetts 02139, USA
[72]Max-Planck-Institut für Physik, 80805 München, Germany
[73a]Institute of Particle Physics, Montréal, Québec, Canada H3A 2T8
[73b]McGill University, Montréal, Québec, Canada H3A 2T8
[74]School of Physics, University of Melbourne, Victoria 3010, Australia
[75a]INFN Sezione di Milano, I-20133 Milano, Italy
[75b]Dipartimento di Fisica, Università di Milano, I-20133 Milano, Italy
[76]University of Mississippi, University, Mississippi 38677, USA
[77]University of Miyazaki, Miyazaki 889-2192, Japan
[78]Université de Montréal, Physique des Particules, Montréal, Québec, Canada H3C 3J7
[79]Moscow Physical Engineering Institute, Moscow 115409, Russian Federation
[80]Moscow Institute of Physics and Technology, Moscow Region 141700, Russian Federation
[81]Graduate School of Science, Nagoya University, Nagoya 464-8602, Japan
[82a]INFN Sezione di Napoli, and Dipartimento di Scienze Fisiche, I-80126 Napoli, Italy
[82b]Università di Napoli Federico II, I-80126 Napoli, Italy
[83]Nara Women's University, Nara 630-8506, Japan
[84]National Central University, Chung-li 32054, Taiwan
[85]National United University, Miao Li 36003, Taiwan
[86]NIKHEF, National Institute for Nuclear Physics and High Energy Physics,
NL-1009 DB Amsterdam, The Netherlands
[87]Department of Physics, National Taiwan University, Taipei 10617, Taiwan
[88]H. Niewodniczanski Institute of Nuclear Physics, Krakow 31-342, Poland

[89]*Nippon Dental University, Niigata 951-8580, Japan*
[90]*Niigata University, Niigata 950-2181, Japan*
[91]*University of Notre Dame, Notre Dame, Indiana 46556, USA*
[92]*Ohio State University, Columbus, Ohio 43210, USA*
[93]*Osaka City University, Osaka 558-8585, Japan*
[94]*Pacific Northwest National Laboratory, Richland, Washington 99352, USA*
[95a]*INFN Sezione di Padova, I-35131 Padova, Italy*
[95b]*Dipartimento di Fisica, Università di Padova, I-35131 Padova, Italy*
[96]*Panjab University, Chandigarh 160014, India*
[97]*Laboratoire de Physique Nucléaire et de Hautes Energies, IN2P3/CNRS, Université Pierre et Marie Curie-Paris6, Université Denis Diderot-Paris7, F-75252 Paris, France*
[98]*Peking University, Beijing 100871, China*
[99a]*INFN Sezione di Perugia, I-06123 Perugia, Italy*
[99b]*Dipartimento di Fisica, Università di Perugia, I-06123 Perugia, Italy*
[100a]*INFN Sezione di Pisa, I-56127 Pisa, Italy*
[100b]*Dipartimento di Fisica, Università di Pisa, I-56127 Pisa, Italy*
[100c]*Scuola Normale Superiore di Pisa, I-56127 Pisa, Italy*
[101]*University of Pittsburgh, Pittsburgh, Pennsylvania 15260, USA*
[102]*Princeton University, Princeton, New Jersey 08544, USA*
[103]*Theoretical Research Division, Nishina Center, RIKEN, Saitama 351-0198, Japan*
[104a]*INFN Sezione di Roma, I-00185 Roma, Italy*
[104b]*Dipartimento di Fisica, Università di Roma La Sapienza, I-00185 Roma, Italy*
[105]*Universität Rostock, D-18051 Rostock, Germany*
[106]*Rutherford Appleton Laboratory, Chilton, Didcot, Oxon, OX11 0QX, United Kingdom*
[107]*CEA, Irfu, SPP, Centre de Saclay, F-91191 Gif-sur-Yvette, France*
[108]*University of Science and Technology of China, Hefei 230026, China*
[109]*Showa Pharmaceutical University, Tokyo 194-8543, Japan*
[110]*Soongsil University, Seoul 156-743, South Korea*
[111]*SLAC National Accelerator Laboratory, Stanford, California 94309 USA*
[112]*University of South Carolina, Columbia, South Carolina 29208, USA*
[113]*Southern Methodist University, Dallas, Texas 75275, USA*
[114]*St. Francis Xavier University, Antigonish, Nova Scotia, Canada B2G 2W5*
[115]*Stanford University, Stanford, California 94305, USA*
[116]*State University of New York, Albany, New York 12222, USA*
[117]*Sungkyunkwan University, Suwon 440-746, South Korea*
[118]*School of Physics, University of Sydney, New South Wales 2006, Australia*
[119]*Department of Physics, Faculty of Science, University of Tabuk, Tabuk 71451, Kingdom of Saudi Arabia*
[120]*Tata Institute of Fundamental Research, Mumbai 400005, India*
[121]*Department of Physics, Technische Universität München, 85748 Garching, Germany*
[122]*Excellence Cluster Universe, Technische Universität München, 85748 Garching, Germany*
[123]*Tel Aviv University, School of Physics and Astronomy, Tel Aviv, 69978, Israel*
[124]*University of Tennessee, Knoxville, Tennessee 37996, USA*
[125]*University of Texas at Austin, Austin, Texas 78712, USA*
[126]*University of Texas at Dallas, Richardson, Texas 75083, USA*
[127]*Toho University, Funabashi 274-8510, Japan*
[128]*Department of Physics, Tohoku University, Sendai 980-8578, Japan*
[129]*Earthquake Research Institute, University of Tokyo, Tokyo 113-0032, Japan*
[130]*Department of Physics, University of Tokyo, Tokyo 113-0033, Japan*
[131]*Tokyo Institute of Technology, Tokyo 152-8550, Japan*
[132]*Tokyo Metropolitan University, Tokyo 192-0397, Japan*
[133a]*INFN Sezione di Torino, I-10125 Torino, Italy*
[133b]*Dipartimento di Fisica, Università di Torino, I-10125 Torino, Italy*
[134]*INFN Sezione di Trieste and Dipartimento di Fisica, Università di Trieste, I-34127 Trieste, Italy*
[135]*IFIC, Universitat de Valencia-CSIC, E-46071 Valencia, Spain*
[136a]*Institute of Particle Physics, Victoria, British Columbia, Canada V8W 3P6*
[136b]*University of Victoria, Victoria, British Columbia, Canada V8W 3P6*
[137]*Virginia Polytechnic Institute and State University, Blacksburg, Virginia 24061, USA*
[138]*Department of Physics, University of Warwick, Coventry CV4 7AL, United Kingdom*
[139]*Wayne State University, Detroit, Michigan 48202, USA*
[140]*University of Wisconsin, Madison, Wisconsin 53706, USA*

[141]Yamagata University, Yamagata 990-8560, Japan
[142]Yonsei University, Seoul 120-749, South Korea

(Received 17 April 2018; published 26 December 2018)

We report measurements of $\sin 2\beta$ and $\cos 2\beta$ using a time-dependent Dalitz plot analysis of $B^0 \to D^{(*)}h^0$ with $D \to K^0_S\pi^+\pi^-$ decays, where the light unflavored and neutral hadron h^0 is a π^0, η, or ω meson. The analysis uses a combination of the final data sets of the *BABAR* and Belle experiments containing 471×10^6 and 772×10^6 $B\bar{B}$ pairs collected at the $\Upsilon(4S)$ resonance at the asymmetric-energy B factories PEP-II at SLAC and KEKB at KEK, respectively. We measure $\sin 2\beta = 0.80 \pm 0.14(\text{stat}) \pm 0.06(\text{syst}) \pm 0.03(\text{model})$ and $\cos 2\beta = 0.91 \pm 0.22(\text{stat}) \pm 0.09(\text{syst}) \pm 0.07(\text{model})$. The result for the direct measurement of the angle is $\beta = (22.5 \pm 4.4(\text{stat}) \pm 1.2(\text{syst}) \pm 0.6(\text{model}))°$. The last quoted uncertainties are due to the composition of the $D^0 \to K^0_S\pi^+\pi^-$ decay amplitude model, which is newly established by a Dalitz plot amplitude analysis of a high-statistics $e^+e^- \to c\bar{c}$ data sample as part of this analysis. We find the first evidence for $\cos 2\beta > 0$ at the level of 3.7 standard deviations. The measurement excludes the trigonometric multifold solution $\pi/2 - \beta = (68.1 \pm 0.7)°$ at the level of 7.3 standard deviations and therefore resolves an ambiguity in the determination of the apex of the CKM Unitarity Triangle. The hypothesis of $\beta = 0°$ is ruled out at the level of 5.1 standard deviations, and thus CP violation is observed in $B^0 \to D^{(*)}h^0$ decays. The measurement assumes no direct CP violation in $B^0 \to D^{(*)}h^0$ decays.

DOI: 10.1103/PhysRevD.98.112012

I. INTRODUCTION

The breaking of CP symmetry is a physical effect with profound consequences, causing particles and antiparticles to behave differently [1–3]. CP violation provides the only possibility to assign matter and antimatter in an absolute and convention-independent way [4]. As one of the Sakharov requirements [5] for baryogenesis, CP violation is a key ingredient in generating, shortly after the big bang, the matter-antimatter asymmetry seen in our present matter-dominated universe. However, CP violation in the standard model (SM) of electroweak interactions is several orders of magnitude too small to account for the observed baryon asymmetry of the Universe [6,7], providing a strong motivation to search for additional sources of CP violation in nature. In the SM, the origin of CP violation is the single irreducible complex phase in the three-family Cabibbo-Kobayashi-Maskawa (CKM) quark-mixing matrix [8,9]. Testing this prediction of the Kobayashi-Maskawa theory [9] was the main objective for the construction and operation of the first-generation asymmetric-energy B factory experiments *BABAR* at SLAC (USA) and Belle at KEK (Japan). *BABAR* and Belle discovered CP violation in the decays of neutral and charged B mesons [10–13] and experimentally confirmed the theoretical predictions in numerous independent measurements [14].

In particular, *BABAR* and Belle observed CP violation in the interference between the direct decays of neutral B mesons into CP eigenstates and these decays after B^0-$\bar{B}^0$ oscillations (referred to as "mixing-induced CP violation") for the "gold plated" decay mode[1] $B^0 \to J/\psi K^0_S$ and other decays mediated by $\bar{b} \to \bar{c}c\bar{s}$ transitions [15,16]. By performing time-dependent CP violation measurements of $\bar{b} \to \bar{c}c\bar{s}$ transitions, *BABAR* and Belle precisely determined the parameter $\sin 2\beta \equiv \sin 2\phi_1$.[2] The angle β of the CKM Unitarity Triangle is defined as $\arg[-V_{cd}V^*_{cb}/V_{td}V^*_{tb}]$, where V_{ij} denotes a CKM matrix element. The current world average measured from $\bar{b} \to \bar{c}c\bar{s}$ transitions is $\sin 2\beta = 0.691 \pm 0.017$ [17], which corresponds to an uncertainty on the angle β of 0.7°. However, there is a twofold trigonometric ambiguity, 2β and $\pi - 2\beta$ (a fourfold ambiguity in β), in inferring the CP-violating weak phase 2β from the measurement of $\sin 2\beta$, and therefore an ambiguity in the determination of the apex of the CKM Unitarity Triangle.

[*]Deceased.
[†]Present address: University of Huddersfield, Huddersfield HD1 3DH, United Kingdom.
[‡]Also at Università di Sassari, I-07100 Sassari, Italy.
[§]Present address: University of South Alabama, Mobile, Alabama 36688, USA.
[¶]Present address: Università di Bologna and INFN Sezione di Bologna, I-47921 Rimini, Italy.
[**]Present address: European Organization for Nuclear Research (CERN), Geneva, Switzerland.
[††]Present address: Wuhan University, Wuhan 430072, China.

[1]In this article the inclusion of charge-conjugated decay modes is implied unless otherwise stated.
[2]*BABAR* uses the notation β and Belle uses ϕ_1; hereinafter β is used.

The trigonometric ambiguity can be resolved experimentally by measuring B meson decays that involve multibody final states. Decay modes such as $B^0 \to J/\psi K^0_S \pi^0$ [18,19], $B^0 \to D^{*+} D^{*-} K^0_S$ [20,21], $B^0 \to K^0_S K^+ K^-$ [22,23], $B^0 \to K^0_S \pi^+ \pi^-$ [24,25], and $B^0 \to D^{(*)} h^0$ with $D \to K^0_S \pi^+ \pi^-$ decays (abbreviated as $B^0 \to [K^0_S \pi^+ \pi^-]^{(*)}_D h^0$) [26–29] enable us to measure $\cos 2\beta$ in addition to $\sin 2\beta$. Although $\sin 2\beta$ is precisely measured, the experimental uncertainties on $\cos 2\beta$ are sizable. Currently, the most precise single measurement has an uncertainty of approximately ± 0.36 on the value of $\cos 2\beta$ [29]. However, no previous single measurement has been sufficiently sensitive to establish the sign of $\cos 2\beta$ that would resolve the trigonometric ambiguity without any assumptions. The most precise direct estimate of the angle β was obtained by a measurement of $B^0 \to K^0_S K^+ K^-$ decays by *BABAR* [22], which resolves the ambiguity at the level of 4.8 standard deviations. However, $B^0 \to K^0_S K^+ K^-$ decays do not provide a theoretically clean probe for the CP-violating weak phase 2β; they only provide access to an effective weak phase $\beta_{\rm eff}$, because at leading order $B^0 \to K^0_S K^+ K^-$ decays are not mediated by tree-level amplitudes, but rather by loop ("penguin") transitions.

An experimentally elegant and powerful approach to accessing $\cos 2\beta$ and thereby resolving the trigonometric ambiguity is provided by $B^0 \to D^{(*)} h^0$ with $D \to K^0_S \pi^+ \pi^-$ decays [26–29], where $h^0 \in \{\pi^0, \eta, \omega\}$ denotes a light unflavored and neutral hadron. The decay $B^0 \to D^* \omega$ is not considered in this analysis. As shown in Fig. 1, the $B^0 \to D^{(*)} h^0$ decay is mediated only by tree-level amplitudes, and to a good approximation only by color-suppressed, CKM-favored $\bar{b} \to \bar{c} u \bar{d}$ tree amplitudes. Additional contributions

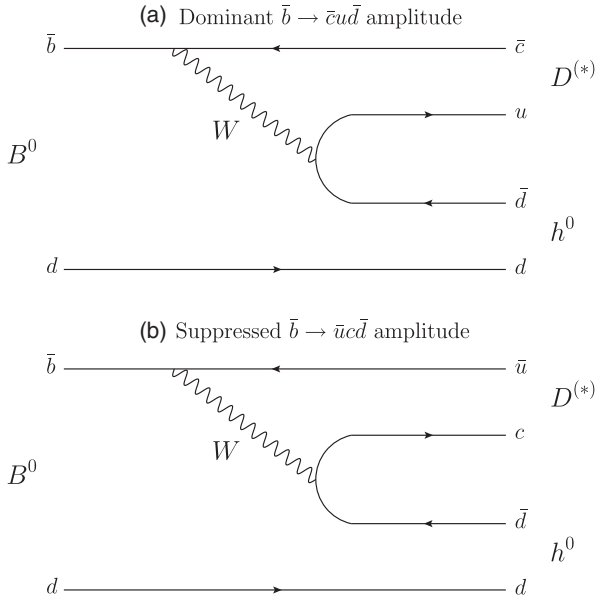

FIG. 1. Feynman diagrams describing $B^0 \to D^{(*)} h^0$ decays: (a) the dominant $\bar{b} \to \bar{c} u \bar{d}$ tree-level amplitudes, and (b) the highly suppressed $\bar{b} \to \bar{u} c \bar{d}$ tree-level amplitudes.

from color-suppressed and doubly Cabibbo-suppressed $\bar{b} \to \bar{u} c \bar{d}$ amplitudes involve different weak phases, but are suppressed by a factor of $|V_{ub} V^*_{cd} / V_{cb} V^*_{ud}| \approx 0.02$ relative to the leading amplitudes, and can be neglected at the experimental sensitivity of the current measurement. The $D^0 \to K^0_S \pi^+ \pi^-$ decay involves complex interference structures that receive resonant and nonresonant contributions from a rich variety of intermediate CP eigenstates and quasi-flavor-specific decays to the three-body final state. If the variations of the relative strong phase as a function of the D^0 meson three-body Dalitz plot phase space are known for $D^0 \to K^0_S \pi^+ \pi^-$ decays, then both $\sin 2\beta$ and $\cos 2\beta$ can be measured from the time evolution of the $B^0 \to [K^0_S \pi^+ \pi^-]^{(*)}_D h^0$ multibody final state [26].

In an $e^+ e^- \to \Upsilon(4S) \to B^0 \bar{B}^0$ event, the time-dependent decay rate of the $B^0 \to [K^0_S \pi^+ \pi^-]^{(*)}_D h^0$ signal decays depends on the D^0 and $\bar{D}^0$ decay amplitudes as a function of the three-body Dalitz plot phase space and on the CP-violating weak phase 2β, and it is proportional to

$$\frac{e^{\frac{-|\Delta t|}{\tau_{B^0}}}}{2} \{ [|\mathcal{A}_{\bar{D}^0}|^2 + |\mathcal{A}_{D^0}|^2] - q(|\mathcal{A}_{\bar{D}^0}|^2 - |\mathcal{A}_{D^0}|^2) \cos(\Delta m_d \Delta t) + 2q\eta_{h^0}(-1)^L \mathrm{Im}(e^{-2i\beta} \mathcal{A}_{D^0} \mathcal{A}^*_{\bar{D}^0}) \sin(\Delta m_d \Delta t) \}. \quad (1)$$

The symbol Δt denotes the proper-time interval between the decays of the two B mesons produced in the $\Upsilon(4S)$ event. The factor $q = +1$ (-1) represents the b-flavor content when the accompanying B meson is tagged as a B^0 ($\bar{B}^0$). The parameters τ_{B^0} and Δm_d are the neutral B meson lifetime and the mass difference between the physical eigenstates of neutral B mesons ("B^0-$\bar{B}^0$ oscillation frequency"), respectively. The quantity $\eta_{h^0} = (-1, -1, +1)$ is the CP eigenvalue of $h^0 = (\pi^0, \eta, \omega)$, and L is the orbital angular momentum of the Dh^0 and $D^* h^0$ system. The relation $\eta_{h^0}(-1)^L$ equals -1 for Dh^0 and $+1$ for $D^* h^0$ ($h^0 \neq \omega$). In this analysis, we consider only $D^* \to D\pi^0$ decays, so an additional factor of -1 that should be included for $D^* \to D\gamma$ decays need not be considered [30]. The D^0 and $\bar{D}^0$ decay amplitudes $\mathcal{A}_{D^0} \equiv \mathcal{A}(M^2_{K^0_S \pi^-}, M^2_{K^0_S \pi^+})$ and $\mathcal{A}_{\bar{D}^0} \equiv \mathcal{A}(M^2_{K^0_S \pi^+}, M^2_{K^0_S \pi^-})$ depend on the position within the $D^0 \to K^0_S \pi^+ \pi^-$ Dalitz plot phase space defined by the Lorentz-invariant variables $M^2_{K^0_S \pi^-} \equiv (p_{K^0_S} + p_{\pi^-})^2$ and $M^2_{K^0_S \pi^+} \equiv (p_{K^0_S} + p_{\pi^+})^2$, where the symbol p_i represents the four-momentum of a final state particle i.

Equation (1) assumes no CP violation in B^0-$\bar{B}^0$ mixing and no direct CP violation in $B^0 \to D^{(*)} h^0$ decays. In our previous time-dependent CP violation analysis that combined *BABAR* and Belle data [31], we determined the parameter $\mathcal{C}$ that measures direct CP violation in two independent samples of $B^0 \to D^{(*)} h^0$ decays. Using D meson decays both to CP eigenstates $D_{CP} \to K^+ K^-, K^0_S \pi^0$, and $K^0_S \omega$, and using the high-statistics control sample

provided by the CKM-favored $\bar{D}^0 \to K^+\pi^-$ decay mode, no evidence for direct CP violation was found in either case [31]. This justifies the assumption of no direct CP violation in $B^0 \to D^{(*)}h^0$ decays for the present measurement.

The last term in Eq. (1) can be rewritten as

$$\mathrm{Im}(e^{-2i\beta}\mathcal{A}_{D^0}\mathcal{A}^*_{\bar{D}^0}) = \mathrm{Im}(\mathcal{A}_{D^0}\mathcal{A}^*_{\bar{D}^0})\cos 2\beta - \mathrm{Re}(\mathcal{A}_{D^0}\mathcal{A}^*_{\bar{D}^0})\sin 2\beta. \quad (2)$$

Equation (2) allows the measurement of $\sin 2\beta$ and $\cos 2\beta$ as independent parameters by a time-dependent Dalitz plot analysis of $B^0 \to D^{(*)}h^0$ with $D \to K^0_S\pi^+\pi^-$ decays.

Although elegant and appealing, the measurements of $\sin 2\beta$ and $\cos 2\beta$ in $B^0 \to D^{(*)}h^0$ with $D \to K^0_S\pi^+\pi^-$ decays are experimentally challenging and technically demanding. The branching fractions of these B and D meson decays are low, at the $\mathcal{O}(10^{-4})$ and $\mathcal{O}(10^{-2})$ level, respectively. These decay modes have neutral particles in the final states that lead to large backgrounds and low reconstruction efficiencies. In addition, we need either a detailed $D^0 \to K^0_S\pi^+\pi^-$ decay amplitude model or other experimental knowledge of the relative strong phase as a function of the D^0 meson three-body Dalitz plot phase space as input to perform the time-dependent Dalitz plot analysis of $B^0 \to D^{(*)}h^0$ with $D \to K^0_S\pi^+\pi^-$ decays.

Time-dependent Dalitz plot analyses of $B^0 \to D^{(*)}h^0$ with $D \to K^0_S\pi^+\pi^-$ decays have been previously performed separately by *BABAR* and Belle. However, neither experiment was sufficiently sensitive to establish CP violation [27–29]. Some of the measurements obtained results far outside of the physical region of the parameter space [27] and used different $D^0 \to K^0_S\pi^+\pi^-$ decay amplitude models [27,28], which complicates the comparison or the combination of the individual results.

In this article, we present measurements of $\sin 2\beta$ and $\cos 2\beta$ by a time-dependent Dalitz plot analysis of $B^0 \to D^{(*)}h^0$ with $D \to K^0_S\pi^+\pi^-$ decays that combines the *BABAR* and Belle data samples, totaling 1.1 ab^{-1} collected at the $\Upsilon(4S)$ resonance. In a recent combined analysis of the related decay, $\bar{B}^0 \to D^{(*)}_{CP}h^0$ with D_{CP} denoting neutral D mesons reconstructed as two-body CP eigenstates, we demonstrated the technical feasibility and the physical advantage of the simultaneous analysis of the data collected by the *BABAR* and Belle experiments [31]. In the present measurement, the benefit is twofold: first, the combination of the *BABAR* and Belle data samples improves the achievable experimental precision by effectively doubling the statistics available for the measurement; second, the combined approach enables common assumptions and applies the same $D^0 \to K^0_S\pi^+\pi^-$ decay amplitude model simultaneously in the analysis of the data collected by both experiments. The approach of combining *BABAR* and Belle data enables unique experimental sensitivity beyond what would be possible by combining two independent measurements, in particular for $\cos 2\beta$. We derive the $D^0 \to K^0_S\pi^+\pi^-$ decay amplitude model from the data by a Dalitz plot amplitude analysis of a high-statistics $e^+e^- \to c\bar{c}$ data sample. This approach ensures full control over the construction and the propagation of uncertainties of the $D^0 \to K^0_S\pi^+\pi^-$ decay amplitude model, and thus enables us to further improve the experimental sensitivity and robustness of the measurement.

The approach of combining the existing data of the B factory experiments *BABAR* and Belle results in measurements from a data sample with an integrated luminosity of more than 1 ab^{-1}. Data samples of comparable size will only be obtained by future heavy flavor experiments: for example, the next-generation high-luminosity B factory experiment Belle II [32], which is expected to collect a data sample of 1 ab^{-1} by the year 2020 and as much as 50 ab^{-1} by 2025. Thus combining the data from the first-generation asymmetric-energy B factory experiments provides not only unique experimental precision, but also demonstrates the discovery potential of Belle II at an early phase of the experiment.

The paper is structured as follows: Section II introduces the *BABAR* and Belle detectors and discusses the data sets used in the present analysis. Section III describes the Dalitz plot amplitude analysis used to determine the $D^0 \to K^0_S\pi^+\pi^-$ decay model from a high-statistics $e^+e^- \to c\bar{c}$ data sample collected by Belle. Section IV presents the measurements of $\sin 2\beta$ and $\cos 2\beta$ by a time-dependent Dalitz plot analysis of $B^0 \to D^{(*)}h^0$ with $D \to K^0_S\pi^+\pi^-$ decays combining the *BABAR* and Belle data sets. Section V describes the significance of the obtained results. Finally, Sec. VI concludes the paper. The paper is accompanied by a letter in Physical Review Letters [33].

II. THE *BABAR* AND BELLE DETECTORS AND DATA SETS

The results presented herein utilize data collected with the *BABAR* detector at the PEP-II e^+e^- storage rings [34] operated at the SLAC National Accelerator Laboratory (Menlo Park, USA) and with the Belle detector at the KEKB e^+e^- storage rings [35] operated at the KEK High Energy Accelerator Research Organization (Tsukuba, Japan). At PEP-II, 3.1 GeV positrons collide on 9 GeV electrons, and at KEKB, 3.5 GeV positrons collide on 8 GeV electrons. The center-of-mass (c.m.) energy of both PEP-II and KEKB is 10.58 GeV, the mass of the $\Upsilon(4S)$ resonance. Due to the asymmetry of the beam energies, the $\Upsilon(4S)$ is produced with a Lorentz boost of $\beta\gamma = 0.560$ at *BABAR* and 0.425 at Belle, allowing measurement of the proper-time interval between the decays of the two B mesons produced in $\Upsilon(4S)$ decays from the displacement of their decay vertices. The design of *BABAR* and Belle as asymmetric-energy B factory experiments is crucial to enable time-dependent CP violation measurements of neutral B mesons, as in the analysis presented in this paper.

The *BABAR* and Belle detectors are large-solid-angle multipurpose magnetic spectrometers, and they are described in detail elsewhere [36–38].

The *BABAR* detector consists of a five-layer, double-sided silicon vertex tracker (SVT), a 40-layer drift chamber (DCH), an internally reflecting ring-imaging Cherenkov detector (DIRC), and a CsI(Tl) crystal electromagnetic calorimeter (EMC) located within a superconducting solenoid magnet that provides a 1.5 T magnetic field. The instrumented flux return (IFR) of the solenoid magnet consists of iron plates interleaved with resistive plate chambers and, in the later runs, limited streamer tubes to detect K_L^0 mesons and to identify muons.

The Belle detector consists of a silicon vertex detector (SVD), a 50-layer central drift chamber (CDC), an array of aerogel threshold Cherenkov counters (ACC), a barrel-like arrangement of time-of-flight scintillation counters (TOF), and an electromagnetic calorimeter comprised of CsI(Tl) crystals (ECL) located inside a superconducting solenoid coil that provides a 1.5 T magnetic field. A steel flux return located outside of the coil is instrumented to detect K_L^0 mesons and to identify muons (KLM). Two inner detector configurations were used. A 2.0 cm radius beampipe and a 3-layer silicon vertex detector were used for the first sample of $152 \times 10^6 B\bar{B}$ pairs, while a 1.5 cm radius beampipe, a 4-layer silicon detector, and a small-cell inner drift chamber were used for the remaining $620 \times 10^6 B\bar{B}$ pairs [39].

The Monte Carlo event generators used at *BABAR* and Belle are based on EvtGen [40], JETSET [41], and Photos [42]. The *BABAR* detector Monte Carlo simulation is based on GEANT4 [43], and the Belle detector Monte Carlo simulation is based on GEANT3 [44].

The first part of the analysis, described in Sec. III, is based on a data sample of 924 fb^{-1} recorded at or near the $\Upsilon(4S)$ and $\Upsilon(5S)$ resonances with the Belle detector [36]. This data set provides a high-statistics sample of $e^+e^- \to c\bar{c}$ events that is used to determine the $D^0 \to K_S^0\pi^+\pi^-$ decay amplitudes. The data set provided by Belle enables a $D^0 \to K_S^0\pi^+\pi^-$ yield that is about three orders of magnitude larger than for the corresponding B meson decay to be studied by the combined *BABAR*+Belle analysis approach. Therefore, the first part of the analysis does not require the combined use of the *BABAR* and Belle data sets.

The second part of the analysis, described in Sec. IV, is based on data samples collected at the $\Upsilon(4S)$ resonance containing $(471 \pm 3) \times 10^6 B\bar{B}$ pairs recorded with the *BABAR* detector and $(772 \pm 11) \times 10^6 B\bar{B}$ pairs recorded with the Belle detector. The combined *BABAR* and Belle data set is used to perform the time-dependent Dalitz plot analysis of $B^0 \to D^{(*)}h^0$ with $D \to K_S^0\pi^+\pi^-$ decays.

III. DETERMINATION OF THE $D^0 \to K_S^0\pi^+\pi^-$ DECAY AMPLITUDES BY DALITZ PLOT AMPLITUDE ANALYSIS USING BELLE $e^+e^- \to c\bar{c}$ DATA

A. Event reconstruction and selection

The $D^{*+} \to D^0\pi_s^+$ candidates are reconstructed from $D^0 \to K_S^0\pi^+\pi^-$ decays and a low momentum ("slow") charged pion π_s^+. The slow pion enables the identification of the production flavor of the neutral D meson, which cannot be inferred directly from the self-conjugate three-body final state. The positive (negative) charge of the $\pi^+{}_s$ determines the flavor of the neutral D meson to be a D^0 ($\bar{D}^0$). Neutral kaons are reconstructed in the decay mode $K_S^0 \to \pi^+\pi^-$, with the invariant mass required to be within 15 MeV/c^2 of the nominal value [45]. Further standard requirements that exploit the displacement of the K_S^0 decay vertex from the interaction point (IP) described in Ref. [46] are applied. For candidates reconstructed from $\Upsilon(4S)$ and $\Upsilon(5S)$ data, requirements of $p^*(D^{*+}) > 2.5$ GeV/c and $p^*(D^{*+}) > 3.1$ GeV/c are applied, respectively, to reject combinatorial background and contamination from B meson decays, where p^* denotes the momentum in the e^+e^- c.m. frame. The decay vertex of D^{*+} candidates is determined by estimating the D^0 meson production vertex from a kinematic fit in which the D^0 meson is constrained to originate from the e^+e^- interaction region. The momentum resolution of soft pions is improved by a kinematic fit in which the $\pi^+{}_s$ is constrained to the determined D^{*+} decay vertex.

The reconstructed charmed meson decays are characterized by two observables: the D^0 candidate mass, M_{D^0}, and the $D^{*+} - D^0$ mass difference, ΔM. Events are selected by requiring $1.825 < M_{D^0} < 1.905$ GeV/c^2 and $140 < \Delta M < 150$ MeV/c^2. For the Dalitz plot fit, a narrower, signal-enhanced region is defined by requiring $(1.865 - 0.015) < M_{D^0} < (1.865 + 0.015)$ GeV/c^2 and $(145.4 - 1.0) < \Delta M < (145.4 + 1.0)$ MeV/c^2. In addition, we define two separate data sideband regions by requiring $1.815 < M_{D^0} < 1.835$ GeV/c^2 and $150.4 < \Delta M < 160.0$ MeV/c^2, and $1.895 < M_{D^0} < 1.915$ GeV/c^2 and $150.4 < \Delta M < 160.0$ MeV/c^2. These data sideband regions are not used in the fit, but provide distributions for the Dalitz plot background description. The two-dimensional ΔM and M_{D^0} data distributions and projections of each observable are shown in Fig. 2.

B. Estimation of the $D^0 \to K_S^0\pi^+\pi^-$ signal and background yields

The signal and background yields are estimated using a two-dimensional unbinned maximum-likelihood (ML) fit to the ΔM and M_{D^0} distributions. In the fit, the shape of the $D^{*+} \to D^0\pi_s^+$ with $D^0 \to K_S^0\pi^+\pi^-$ signal decays is parametrized by the sum of four two-piece normal distributions for M_{D^0} and by the sum of a normal distribution, a Johnson's SU function [47], a two-piece normal distribution, and a threshold function of the form $(\Delta M - M_{\pi^+})^{1/2} + a(\Delta M - M_{\pi^+})^{3/2} + b(\Delta M - M_{\pi^+})^{5/2}$ for ΔM. The width of the reconstructed ΔM distribution depends on the D^0 candidate mass. The ΔM distribution tends to become broader as the reconstructed D^0 mass deviates from the M_{D^0} peak position. To account for this correlation, the ΔM distribution is constructed using a conditional probability

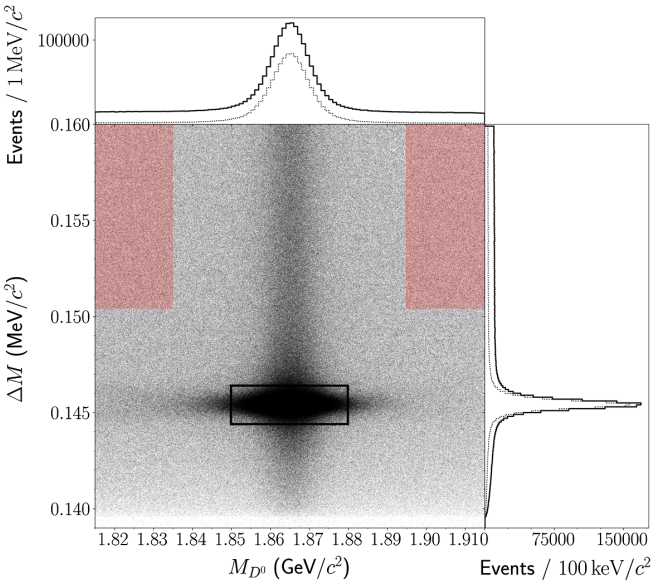

FIG. 2. Two-dimensional ΔM and M_{D^0} data distributions for $D^{*+} \to D^0\pi_s^+$ with $D^0 \to K_S^0\pi^+\pi^-$ decays reconstructed from Belle $e^+e^- \to c\bar{c}$ data, and the definitions of the signal (open black rectangle) and sideband regions (filled red rectangles). The histograms on the top and at the right show one-dimensional projections for M_{D^0} and ΔM, respectively. In the histograms, solid lines indicate projections for one observable within the full range of the other observable, and dashed lines represent projections in which the other observable is required to be within the signal region.

density function (p.d.f.) that scales the ΔM width with a fourth-order polynomial function that has the deviation of the reconstructed M_{D^0} from the M_{D^0} peak position as argument. In the fit, the fractions and widths of the tail components relative to those of the core components are fixed to values estimated using MC simulations, and the fractions and widths of the core components are determined by the fit.

The following four separate categories are considered for the background.

The first source of background arises from the combination of correctly reconstructed $D^0 \to K_S^0\pi^+\pi^-$ candidates with random tracks during reconstruction. This "random slow pion" background has the same M_{D^0} shape as the signal, but the ΔM shape follows a smooth phase space distribution that is parametrized by a threshold function.

The second background category is composed of real π_+^s from $D^{*+} \to D^0\pi_s^+$ decays that are combined with wrong D^0 candidates formed from random tracks or with misreconstructed real D^0 decays. The distribution of this "real slow pion" background is mainly flat in M_{D^0} and very broad in ΔM due to the reconstruction of wrong D^0 candidates, but receives a small contribution that peaks in ΔM but is broad in M_{D^0} due to misreconstructed real D^0 decays. The shape of the background for wrong D^0 candidates is parametrized by a first-order polynomial function and a threshold function in M_{D^0} and ΔM, respectively; that for misreconstructed real D^0 decays is parametrized by a Crystal Ball function [48] and a Johnson's SU function for M_{D^0} and ΔM, respectively.

The third background category contains background from D^0 decay modes that have the same final state as $D^0 \to K_S^0\pi^+\pi^-$ decays, e.g., $D^0 \to \pi^+\pi^-\pi^+\pi^-$ and $D^0 \to K_S^0K_S^0$ decays. The $D^0 \to \pi^+\pi^-\pi^+\pi^-$ decays are effectively removed by the applied K_S^0 selection, and $D^0 \to K_S^0K_S^0$ decays have a very small branching fraction of $\mathcal{O}(10^{-4})$. This "$D^0 \to 4\pi$" background is parametrized by two Gaussian functions for M_{D^0} and the sum of a Gaussian function and a Johnson's SU function for ΔM. This background is at the subpercent level relative to the signal. The fraction of this background is fixed to the expectation value obtained from Monte Carlo (MC) simulations.

The fourth background category accounts for the remaining combinatorial background originating from random combinations of tracks. This "combinatorial background" is parametrized by a first-order polynomial function in M_{D^0} and a threshold function in ΔM.

In the two-dimensional fit of the ΔM and M_{D^0} distributions, a total yield of 1217300 ± 2000 signal events is obtained. The signal purity is 94% in the signal-enhanced region used to extract the $D^0 \to K_S^0\pi^+\pi^-$ decay amplitude parameters. The results of the fit are summarized in Table I. The ΔM and M_{D^0} data distributions and projections of the fit are shown in Fig. 3.

C. Dalitz plot amplitude analysis

The $D^0 \to K_S^0\pi^+\pi^-$ decay can proceed via a rich variety of intermediate two-body (resonant) or three-body (nonresonant) channels. The contributions exhibit complex interference phenomena that are observable as characteristic patterns in the three-body Dalitz plot phase space as shown in Fig. 4. A Dalitz plot amplitude analysis is performed to disentangle and quantify the individual contributions.

1. Dalitz plot amplitude model

The $D^0 \to K_S^0\pi^+\pi^-$ decay amplitude is parametrized by a combination of the isobar ansatz [49] with the K-matrix

TABLE I. Signal and background yields determined by a two-dimensional fit to the M_{D^0} and ΔM distributions of $D^{*+} \to D^0\pi_s^+$ with $D^0 \to K_S^0\pi^+\pi^-$ decays reconstructed from Belle $e^+e^- \to c\bar{c}$ data.

Component	Yield
$D^{*+} \to D^0\pi_s^+$ with $D^0 \to K_S^0\pi^+\pi^-$ signal	$1\,217\,300 \pm 2\,000$
Background containing real D^0 and random slow pions	$61\,330 \pm 1\,280$
Background containing real slow pions and wrong D^0	$249\,700 \pm 10\,000$
Background from $D^0 \to 4\pi$	3 400 (fixed)
Combinatorial background	$271\,000 \pm 9\,000$

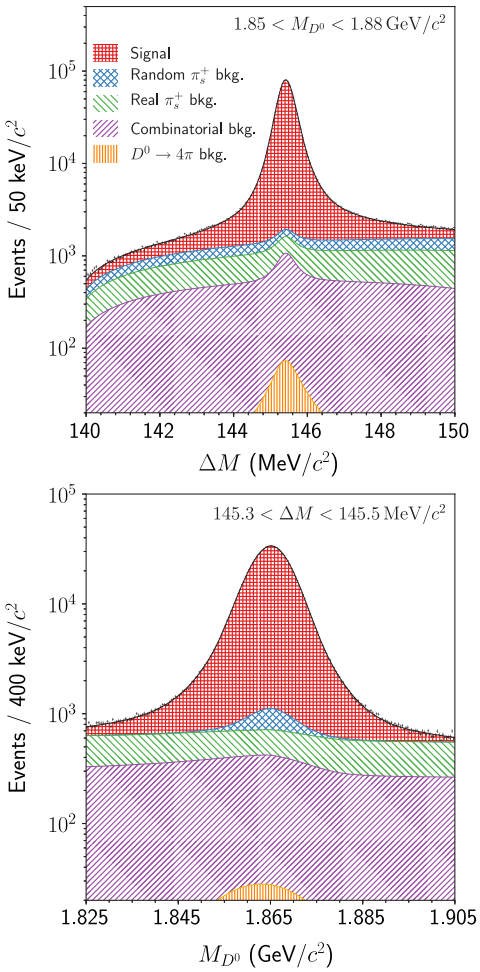

FIG. 3. Data distributions of ΔM and M_{D^0} for $D^{*+} \to D^0\pi_s^+$ with $D^0 \to K_S^0\pi^+\pi^-$ decays reconstructed from Belle $e^+e^- \to c\bar{c}$ data (points with error bars), and projections of the signal and background components of the fit (lines and shaded areas) as indicated in the legend. In plotting the ΔM and M_{D^0} distributions $1.85 < M_{D^0} < 1.88$ GeV/c^2 and $145.3 < M_{D^0} < 145.5$ MeV/c^2 are required, respectively, to select signal-enhanced regions.

formalism [50] for the $\pi\pi$ S-wave and the LASS parametrization [51] for the $K\pi$ S-wave:

$$\mathcal{A}(M^2_{K^0_S\pi^-}, M^2_{K^0_S\pi^+}) = \sum_{r\neq(K\pi/\pi\pi)_{L=0}} a_r e^{i\phi_r}\mathcal{A}_r(M^2_{K^0_S\pi^-}, M^2_{K^0_S\pi^+}) + F_1(M^2_{\pi^+\pi^-}) + \mathcal{A}_{K\pi_{L=0}}(M^2_{K^0_S\pi^-}) + \mathcal{A}_{K\pi_{L=0}}(M^2_{K^0_S\pi^+}). \quad (3)$$

In the isobar ansatz, the two-body $\pi\pi$ and $K\pi$ resonant channels with nonzero angular momentum are parametrized by a coherent sum of the contributing intermediate quasi-two-body amplitudes. In the coherent sum, the rth intermediate quasi-two-body amplitude $\mathcal{A}_r$ enters with magnitude a_r and relative phase ϕ_r. The symbol F_1 denotes the decay amplitude for the $\pi\pi$ S-wave contributions parametrized by the K-matrix approach. The symbol $\mathcal{A}_{K\pi_{L=0}}$ denotes the amplitude for the $K\pi$ S-wave contribution using the LASS parametrization. In Eq. (3), no additional nonresonant term is included, because the K-matrix approach and the LASS parametrization naturally account for the nonresonant three-body contributions in the $\pi\pi$ and $K\pi$ systems, respectively.

a. Isobar ansatz. In the isobar ansatz, the quasi-two-body amplitude for a neutral D meson decaying via the rth intermediate resonance $(h_1h_2)_r$ with spin L to the three-body final state $h_1h_2h_3$ can be written as

$$A_r(M^2_{K^0_S\pi^-}, M^2_{K^0_S\pi^+}) = F_D^{(L)}(q, q_0) \times F_r^{(L)}(p, p_0) \times Z_L(\Omega) \times T_r(m), \quad (4)$$

where the terms are described below.

The form factors $F_D^{(L)}$ and $F_r^{(L)}$ describe the production $D \to rh_3$ and the decay $r \to h_1h_2$ of the resonance r and the daughters of the resonance, respectively. The form factors are parametrized as Blatt-Weisskopf barrier penetration factors [52] that account for spin-dependent effects and prevent the decay amplitudes from diverging for large momentum transfers. The form factors depend on the momentum q (p) of the bachelor particle h_3 (one of the resonance's daughter particles h_1 or h_2) evaluated in the resonance rest frame, and q_0 (p_0) is the value of q (p) when the invariant mass equals the pole mass of the resonance. The Blatt-Weisskopf barrier penetration factors are defined as

$$L = 0\colon\ F^{(0)}(z, z_0) = 1, \quad (5)$$

$$L = 1\colon\ F^{(1)}(z, z_0) = \sqrt{\frac{1+z_0}{1+z}}, \quad (6)$$

$$L = 2\colon\ F^{(2)}(z, z_0) = \sqrt{\frac{(z_0-3)^2+9z_0}{(z-3)^2+9z}}, \quad (7)$$

where $z = (|q|d)^2$ and $z_0 = (|q_0|d)^2$. The parameter d represents the meson radius or the impact parameter of the decay particles for the D meson d_D and the resonances d_r, respectively. In the present analysis, $d_D = 5\hbar c/\mathrm{GeV} \approx 1$ fm and $d_r = 1.5\hbar c/\mathrm{GeV} \approx 0.3$ fm are applied.

The Zemach formalism [53] describes the angular components of the amplitudes using a spin-tensor approach to express the angular correlations among the final state particles by the function $Z_L(\Omega)$, where the symbol Ω represents the angular relations of the involved particles.

The propagator term T_r describes the dynamics in the resonance decay. In this analysis, the term is parametrized by a relativistic Breit-Wigner (BW) line-shape function defined as

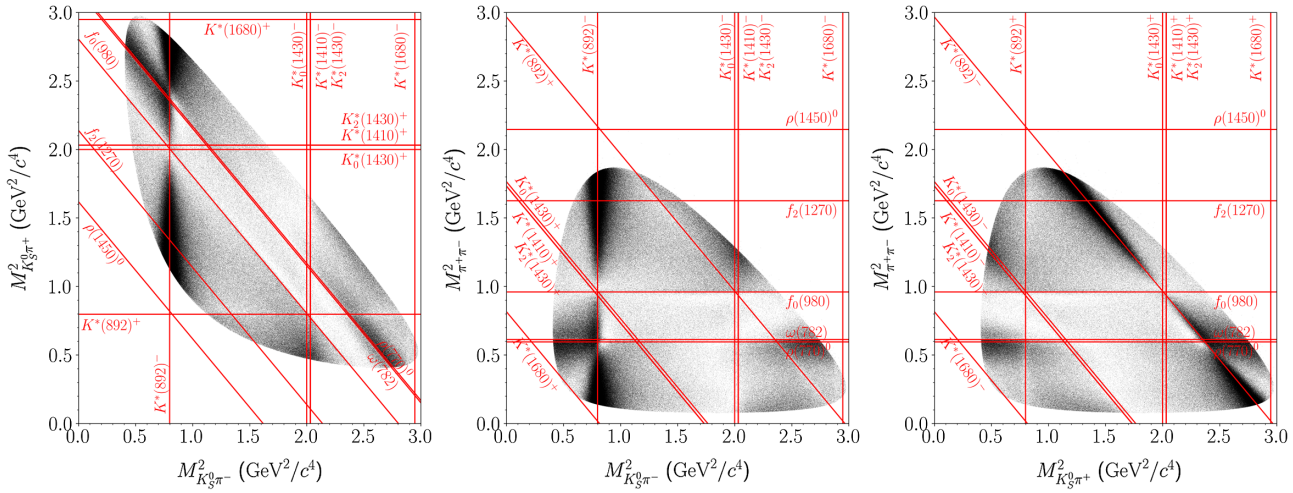

FIG. 4. Dalitz plot data distributions for all three combinations of $M^2_{K^0_S\pi^-}$, $M^2_{K^0_S\pi^+}$, and $M^2_{\pi^+\pi^-}$ for $D^0 \to K^0_S\pi^+\pi^-$ from $D^{*+} \to D^0\pi^+_s$ decays reconstructed from Belle $e^+e^- \to c\bar{c}$ data. For illustration purposes, the approximate locations of various intermediate two-body resonances are indicated by horizontal, vertical, and diagonal lines.

$$T_r(m) = \frac{1}{m_0^2 - m^2 - im_0\Gamma(m)}, \tag{8}$$

where m_0 denotes the pole mass of the resonance, and the mass-dependent width Γ is given by

$$\Gamma(m) = \Gamma_0\left(\frac{q}{q_0}\right)^{(2L+1)}\left(\frac{m_0}{m}\right)F_r^{(L)2}. \tag{9}$$

The isobar ansatz parametrizes the P- and D-wave contributions to the $D^0 \to K^0_S\pi^+\pi^-$ decay. In the nominal Dalitz plot amplitude model, the following intermediate quasi-two-body resonances are included: the Cabibbo-favored $K^*(892)^-\pi^+$, $K_2^*(1430)^-\pi^+$, $K^*(1680)^-\pi^+$, $K^*(1410)^-\pi^+$ channels; the doubly Cabibbo-suppressed $K^*(892)^+\pi^-$, $K_2^*(1430)^+\pi^-$, $K^*(1410)^+\pi^-$ modes; and the CP eigenstates $K^0_S\rho(770)^0$, $K^0_S\omega(782)$, $K^0_Sf_2(1270)$, and $K^0_S\rho(1450)^0$. To reduce the complexity of the Dalitz plot amplitude analysis, masses and widths are fixed to the world averages [45] for all resonances except for the $K^*(892)^\pm$, for which the parameters are free to vary in the fit.

b. K-matrix formalism. The K-matrix formalism is particularly suitable to describe the $J^{PC} = 0^{++}$ scalar contributions to the complex S-wave dynamics occurring in the $\pi^+\pi^-$ system of $D^0 \to K^0_S\pi^+\pi^-$ decays. It preserves unitarity in the presence of overlapping resonances and coupled channels [49]. The *BABAR*, Belle, and LHCb experiments have employed the K-matrix approach in Dalitz plot amplitude analyses of $D^0 \to K^0_S\pi^+\pi^-$ decays to perform measurements of D^0-$\bar{D}^0$ oscillations [54,55] and measurements of the Unitarity Triangle angle γ [56] in B meson decays [57,58]. Following the previous measurements, we apply the K-matrix formalism in the P-vector approximation [59] to model the $\pi\pi$ S-wave contribution to the $D^0 \to K^0_S\pi^+\pi^-$ decay.

In this parametrization, the decay amplitude F_1 entering in Eq. (3) as the contribution of the $\pi\pi$ S-wave is defined by the relation

$$F_i(s) = [I - iK(s)\rho(s)]^{-1}_{ij}P_j(s), \tag{10}$$

where the indices i and j denote the particular channels ($1 = \pi\pi$, $2 = K\bar{K}$, $3 = \pi\pi\pi\pi$, $4 = \eta\eta$, and $5 = \eta\eta'$) contributing to the scattering process. The production vector $P(s)$, where s is the square of the invariant mass of the $\pi^+\pi^-$ system, parametrizes the initial production of states into the open channels, and the K-matrix describes the scattering process. In this analysis, only the $\pi^+\pi^-$ final states are considered. The term I is the identity matrix. The phase space matrix ρ controls the threshold singularities of the amplitude, and the matrix elements for the two-body and multi-meson channels are defined in Ref. [60]. The K-matrix is defined as

$$K_{ij}(s) = \left(f_{ij}^{\text{scatt}}\frac{1 - s_0^{\text{scatt}}}{s - s_0^{\text{scatt}}} + \sum_\alpha \frac{g_i^\alpha g_j^\alpha}{m_\alpha^2 - s}\right)f_{A0}(s). \tag{11}$$

The parameters m_α are the physical poles of the K-matrix, while g_i^α are the coupling constants of the ith channel to the pole α. The parameters f_{ij}^{scatt} and s_0^{scatt} describe the smooth, slowly varying part of the K-matrix. Units of GeV$^2/c^4$ are implied for the number 1. The symbol f_{A0} is the so-called "Adler zero" factor, defined as

$$f_{A0}(s) = \frac{1 - s_{A0}}{s - s_{A0}}\left(s - s_A\frac{m_\pi^2}{2}\right). \tag{12}$$

The Adler zero factor suppresses the false kinematic singularity at $s = 0$ in the physical region close to the $\pi^+\pi^-$ threshold [61].

TABLE II. The K-matrix parameters estimated by a global analysis of available $\pi\pi$ scattering data (taken from Refs. [57,60]). The units of the pole masses m_α and the coupling constants g_i^α are in GeV/c^2. The units of $s_0^{\rm scatt}$ and s_{A0} are GeV$^2/c^4$, while s_A is dimensionless.

m_α	$g^\alpha_{\pi^+\pi^-}$	$g^\alpha_{K\bar{K}}$	$g^\alpha_{4\pi}$	$g^\alpha_{\eta\eta}$	$g^\alpha_{\eta\eta'}$
0.651 00	0.228 89	−0.553 77	0.000 00	−0.398 99	−0.346 39
1.203 60	0.941 28	0.550 95	0.000 00	0.390 65	0.315 03
1.558 17	0.368 56	0.238 88	0.556 39	0.183 40	0.186 81
1.210 00	0.336 50	0.409 07	0.856 79	0.199 06	−0.009 84
1.822 06	0.181 71	−0.175 58	−0.796 58	−0.003 55	0.223 58
	$f_{11}^{\rm scatt}$	$f_{12}^{\rm scatt}$	$f_{13}^{\rm scatt}$	$f_{14}^{\rm scatt}$	$f_{15}^{\rm scatt}$
	0.233 99	0.150 44	−0.205 45	0.328 25	0.354 12
$s_0^{\rm scatt}$	s_{A0}	s_A			
−3.926 37	−0.15	1			

The production vector P has the same pole structure as the K-matrix and is defined as

$$P_j(s) = f_{1j}^{\rm prod}\frac{1-s_0^{\rm prod}}{s-s_0^{\rm prod}} + \sum_\alpha \frac{\beta_\alpha g_j^\alpha}{m_\alpha^2 - s}. \quad (13)$$

The β_α are the complex production couplings, and the parameters $f_{1j}^{\rm prod}$ and $s_0^{\rm prod}$ describe the production of the slowly varying part of the K-matrix.

In this analysis, the K-matrix parameters m_α, g_i^α, $f_{ij}^{\rm scatt}$, $s_0^{\rm scatt}$, s_{A0}, and s_A are fixed to the results of a global analysis of available $\pi\pi$ scattering data [57,60] as summarized in Table II. The complex production couplings β_α and the production parameters $f_{1j}^{\rm prod}$ are free parameters determined from the fit.

c. LASS parametrization. For the $K\pi$ S-wave, an approach introduced by the LASS Collaboration to describe $K^-\pi^+$ scattering processes is applied [51]. The Cabibbo-favored $K_0^*(1430)^-$ and the doubly Cabibbo-suppressed $K_0^*(1430)^+$ contributions are each described by the empirical LASS parametrization, which is constructed from a BW term for the $K_0^*(1430)$ and a nonresonant component having an effective range and that introduces a phase shift:

$$\mathcal{A}_{K\pi_{L=0}}(s) = R\sin\delta_R e^{i\delta_R}e^{i2\delta_F} + F\sin\delta_F e^{i\delta_F}, \quad (14)$$

where

$$\delta_R = \phi_R + \tan^{-1}\left[\frac{M\Gamma(m_{K\pi}^2)}{M^2 - m_{K\pi}^2}\right], \quad (15)$$

$$\delta_F = \phi_F + \cot^{-1}\left[\frac{1}{aq} + \frac{rq}{2}\right]. \quad (16)$$

The parameters R, ϕ_R, F and ϕ_F are the amplitudes and phases of the resonant and nonresonant components. The parameters a and r are the scattering length and the effective interaction length, and q is the momentum of the spectator particle in the $K\pi$ rest frame. The parameters M and $\Gamma(M_{K\pi}^2)$ are the mass and the mass-dependent width of the resonant term defined in Eq. (9); the phases δ_R and δ_F depend on $m_{K\pi}^2$. The mass and the width of the $K_0^*(1430)^\pm$ and the parameters R, ϕ_R, F, ϕ_F, a, and r are determined by the fit. The LASS parameters for the Cabibbo-favored $K_0^*(1430)^-$ and the doubly Cabibbo-suppressed $K_0^*(1430)^+$ contributions are assumed to be identical.

2. Dalitz plot reconstruction efficiency correction

Experimental effects, such as detector acceptance variations, reconstruction algorithms, or the event selection criteria, can produce nonuniformities in the reconstruction efficiency as a function of the Dalitz plot phase space, $\epsilon(M^2_{K^0_S\pi^-}, M^2_{K^0_S\pi^+})$. To account for these effects in the Dalitz amplitude analysis, the efficiency variations are estimated using a high-statistics sample of MC events of inclusive $e^+e^- \to c\bar{c}$ decays that contain the $D^{*+} \to D^0\pi^+{}_s$, with $D^0 \to K^0_S\pi^+\pi^-$, signal decays. In the MC simulations, the $D^0 \to K^0_S\pi^+\pi^-$ decay is generated uniformly in the available D meson decay phase space in order to uniformly populate the Dalitz plot. The generated decays are passed to a GEANT3-based simulation with a specific Belle configuration to simulate the detector response.

The simulated detector response then undergoes the same reconstruction algorithms and event selection requirements as the data. The generated MC sample contains 50×10^6 $D^{*+} \to D^0\pi^+{}_s$, $D^0 \to K^0_S\pi^+\pi^-$ signal decays, approximately 50 times the signal data, which allows us to construct a detailed map of the reconstruction efficiency across the Dalitz plot.

The efficiency map is constructed using an approach *BABAR* introduced in the search for the $Z(4430)^-$ state [62]. In this approach, the efficiency is expressed as a function of

the square of the two-body invariant mass $M^2_{K^0_S\pi^-}$ and $\cos\theta_{K^0_S}$. The variable $\cos\theta_{K^0_S}$ is computed as the normalized dot product between the $K^0_S\pi^-$ three-momentum vector measured in the D meson rest frame and the three-momentum vector of the K^0_S meson after a Lorentz transformation from the D meson rest frame to the $K^0_S\pi^-$ rest frame. This choice of variables naturally introduces a "rectangular Dalitz plot" that is insensitive to potential binning effects that may arise at the curved edges of the $M^2_{K^0_S\pi^-}$ and $M^2_{\pi^+\pi^-}$ Dalitz phase space due to the finite MC sample statistics. In order to parametrize the reconstruction efficiency and to smooth statistical fluctuations, the efficiency map is constructed as follows.

In the first step, the angular variations of the efficiency are estimated by expanding the $\cos\theta_{K^0_S}$ distributions by a linear combination of Legendre polynomials up to order $L = 7$:

$$\epsilon(\cos\theta_{K^0_S}) = \sum_{L=0}^{7} c_L(M^2_{K^0_S\pi^-}) Y^0_L(\cos\theta_{K^0_S}). \quad (17)$$

The mass-squared dependent coefficients c_L are estimated by fitting the linear combination of Legendre polynomials to the $\cos\theta_{K^0_S}$ distributions in intervals of $M^2_{K^0_S\pi^-}$. This forms, for each of the eight coefficients $c_0, c_1, ..., c_7$, a distribution as a function of $M^2_{K^0_S\pi^-}$. In the second step, each of the c_L distributions is fit as a function of $M^2_{K^0_S\pi^-}$. The coefficient c_0 is modeled by a fifth-order polynomial function multiplied with a sigmoid function. This choice of parametrization enables us to properly describe the drop in the reconstruction efficiency near the upper boundary of $M^2_{K^0_S\pi^-}$. The coefficients $c_1, c_2, ..., c_7$ are fit by fifth-order Chebyshev polynomial functions.

The chosen order L of the polynomial functions has been found to be high enough to describe the details of the efficiency variations, and at the same time to be low enough to avoid overfitting any structures. The dependence on the chosen order of the expansion in linear combinations of Legendre polynomials is weak; lower or higher choices than $L = 7$ yield consistent results.

The reconstruction efficiency is nearly flat over large parts of the Dalitz plot phase space. The efficiency decreases slightly at larger values of $M^2_{K^0_S\pi^-}$ and drops close to the kinematic border. The two-dimensional binned distributions of the reconstruction efficiency and the resulting parametrized efficiency maps are shown as a function of $M^2_{K^0_S\pi^-}$ and $M^2_{\pi^+\pi^-}$, and of $M^2_{K^0_S\pi^-}$ and $\cos\theta_{K^0_S}$, in Fig. 5. The efficiency map well represents the variations of the reconstruction efficiency over the full Dalitz plot phase

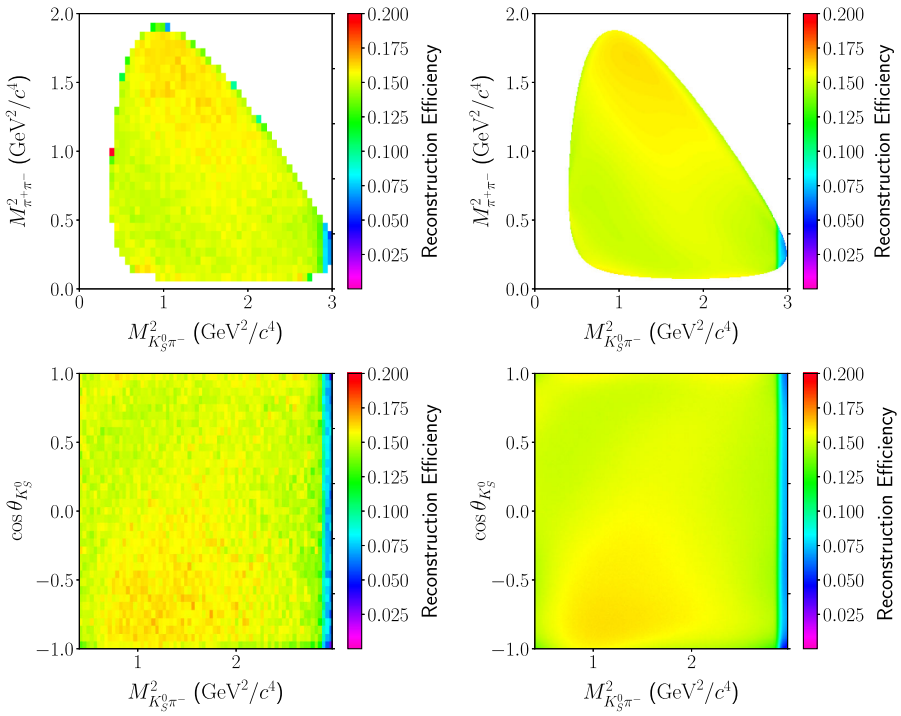

FIG. 5. Variation of the Dalitz plot reconstruction efficiency as a function of $M^2_{K^0_S\pi^-}$ and $M^2_{\pi^+\pi^-}$ (top), and as a function of $M^2_{K^0_S\pi^-}$ and $\cos\theta_{K^0_S}$ (bottom). The efficiency variations are estimated using a high-statistics sample of Monte Carlo events of inclusive $e^+e^- \to c\bar{c}$ decays containing $D^{*+} \to D^0\pi^+_s$ with $D^0 \to K^0_S\pi^+\pi^-$ signal decays (left), and detailed efficiency maps (right) are constructed by the parametrized model described in Sec. III C 2.

space, including the efficiency drops at the kinematic edges of the Dalitz plot. The binned distributions of the reconstruction efficiency are compared to the parametrized efficiency map, and a reduced χ^2 of 1.03 is obtained for 2450 degrees of freedom (d.o.f.).

3. Dalitz plot background description

The Dalitz plot distributions of the background are estimated from the data using two $M_{D^0} - \Delta M$ sideband regions defined by $1.815 < M_{D^0} < 1.835$ GeV/c^2 and $150.4 < \Delta M < 160.0$ MeV/c^2, and $1.895 < M_{D^0} < 1.915$ GeV/c^2 and $150.4 < \Delta M < 160.0$ MeV/c^2. The distribution of the background has a smooth shape over the Dalitz plot. The background exhibits small resonant contributions from the $K^*(892)^-$, $K^*(1680)^-$, and $\rho(770)$ resonances, and further contributions from the $K_0^*(1430)^-$, $K_2^*(1430)^-$, and $K^*(1410)^-$ resonances, which appear as a single broad enhancement. In order to reduce the sensitivity to statistical fluctuations due to the finite sample statistics in the data sideband regions, a parametrized model of the background in the sidebands is constructed and fitted to the Dalitz plot distributions. The background model is composed of a sixth-order polynomial function for the smooth distributions and BW line-shapes for the $K^*(892)^-$, $K^*(1680)^-$, and $\rho(770)^0$ resonances and for the mixture of excited kaon states at approximately 1410 MeV/c^2. These resonant contributions are added incoherently. The background model provides an accurate description of the background in all regions of the Dalitz plot phase space.

4. Likelihood function and procedure for the $D^0 \to K^0_S\pi^+\pi^-$ Dalitz plot fit

The $D^0 \to K^0_S\pi^+\pi^-$ decay amplitude parameters are estimated using an unbinned ML fit to the Dalitz plot distributions of the flavor-tagged D^0 sample. The likelihood function, accounting for the contributions of the signal and background, is written as

$$\begin{aligned}\mathcal{L} = \prod_{i=1}^{N} [& f_{\rm sig} \times p_{\rm sig}(M^2_{K^0_S\pi^-}, M^2_{K^0_S\pi^+}) \\ & + (1 - f_{\rm sig}) \times (f_{\rm rnd} \times p_{\rm rnd}(M^2_{K^0_S\pi^-}, M^2_{K^0_S\pi^+}) \\ & + (1 - f_{\rm rnd}) \times p_{\rm bkg}(M^2_{K^0_S\pi^-}, M^2_{K^0_S\pi^+}))], \end{aligned} \tag{18}$$

where the index i runs over the reconstructed $D^0 \to K^0_S\pi^+\pi^-$ candidates. The signal fraction $f_{\rm sig}$ and the fraction of the random slow pion background $f_{\rm rnd}$ are determined by the two-dimensional fit to the M_{D^0} and ΔM distributions. The functions $p_{\rm sig}$, $p_{\rm rnd}$, and $p_{\rm bkg}$ are the p.d.f.s of the Dalitz plot distributions for the signal, the random slow pion background, and the remaining background, respectively. The signal p.d.f. is constructed from the efficiency-corrected Dalitz plot intensities, computed from the absolute square of the $D^0 \to K^0_S\pi^+\pi^-$ decay amplitude $\mathcal{A}(M^2_{K^0_S\pi^-}, M^2_{K^0_S\pi^+})$ defined in Eq. (3), and by normalizing to the available Dalitz plot phase space:

$$p_{\rm sig}(M^2_{K^0_S\pi^-}, M^2_{K^0_S\pi^+}) = \frac{\epsilon(M^2_{K^0_S\pi^-}, M^2_{K^0_S\pi^+})|\mathcal{A}(M^2_{K^0_S\pi^-}, M^2_{K^0_S\pi^+})|^2}{\int_D \epsilon(M^2_{K^0_S\pi^-}, M^2_{K^0_S\pi^+})|\mathcal{A}(M^2_{K^0_S\pi^-}, M^2_{K^0_S\pi^+})|^2 dM^2_{K^0_S\pi^-} dM^2_{K^0_S\pi^+}}. \tag{19}$$

The random slow pion background is composed of a mixture of real D^0 and $\bar{D}^0$ mesons decaying to the $K^0_S\pi^+\pi^-$ final state. During the reconstruction of $D^{*+} \to D^0\pi^+_s$ decays, these D mesons are combined with random slow pion candidates. If the slow pion has the incorrect charge, the c-flavor content of the neutral D meson will be misidentified, and the wrong flavor will be assigned. Neglecting possible production or detection asymmetries, the naïve expectation of the probability to select a slow pion track with the wrong charge is $p = 0.5$. The decay amplitudes for D^0 and $\bar{D}^0$ mesons are related by an exchange of the Dalitz plot variables, $\mathcal{A}_{D^0} = \mathcal{A}(M^2_{K^0_S\pi^-}, M^2_{K^0_S\pi^+}) \leftrightarrow \mathcal{A}_{\bar{D}^0} = \mathcal{A}(M^2_{K^0_S\pi^+}, M^2_{K^0_S\pi^-})$. The p.d.f. of the random slow pion background is constructed from the signal p.d.f. by allowing for the exchange of the Dalitz plot positions and is defined as

$$\begin{aligned} & p_{\rm rnd}(M^2_{K^0_S\pi^-}, M^2_{K^0_S\pi^+}) \\ & \quad = (1 - f_{\rm wtag}) \times p_{\rm sig}(M^2_{K^0_S\pi^-}, M^2_{K^0_S\pi^+}) \\ & \qquad + f_{\rm wtag} \times p_{\rm sig}(M^2_{K^0_S\pi^+}, M^2_{K^0_S\pi^-}). \end{aligned} \tag{20}$$

The fraction of "wrong D meson flavor-tags," $f_{\rm wtag}$, is estimated directly from the data by a separate Dalitz plot fit to the $150 < \Delta M < 155$ MeV/c^2 sideband region that has no signal, but has an enhanced population from the random slow pion background. In this Dalitz plot fit to the data sideband, the fraction of wrong D meson flavor-tags is measured to be $f_{\rm wtag} = 0.492 \pm 0.075$, in agreement with the naïve expectation. In the subsequent Dalitz plot fit to the signal region, $f_{\rm wtag}$ is fixed to the estimate obtained from the sideband.

The background p.d.f. $p_{\rm bkg}$ is constructed from the parametrized background model described in Sec. III C 3. The background is composed of combinatorial background and additional contributions from processes containing real slow pions and wrong D^0 mesons.

Due to the high statistics of the Belle $e^+e^- \to c\bar{c}$ data sample of more than 10^6 events, and the complexity of the $D^0 \to K^0_S\pi^+\pi^-$ decay amplitude model, maximizing the likelihood function and performing the Dalitz plot fit is computationally intensive, taking hours to days on a single CPU core of a recent Intel Xeon processor-based Linux workstation. A new software framework for Dalitz plot amplitude analyses has therefore been developed to increase the performance of the fit and to realize this analysis. Key features of the framework are the parallel computing algorithms for both the evaluation of the likelihood function defined in Eq. (18) and the numerical integration of the p.d.f.s. The parallel computing algorithms, realized using OpenMP [63,64], enable the Dalitz plot fits to make simultaneous use of multiple CPUs to significantly reduce the required run time. Using 64 CPU cores, the time needed to reach convergence of the fit has been reduced by a factor of 40.

The $D^0 \to K^0_S\pi^+\pi^-$ decay amplitude parameters are determined by maximizing Eq. (18) for the Dalitz plot distributions in the signal-enhanced region defined in Sec. III A. The amplitude magnitudes a_r and phases ϕ_r of the intermediate resonant states are free parameters in the fit, measured relative to the $K^0_S\rho(770)^0$ amplitude. The $K^0_S\rho(770)^0$ amplitude is fixed to $a_{K^0_S\rho(770)^0} = 1$ and $\phi_{K^0_S\rho(770)^0} = 0°$ and serves as a reference.

5. Results of the $D^0 \to K^0_S\pi^+\pi^-$ Dalitz plot amplitude analysis

The results for the estimated $D^0 \to K^0_S\pi^+\pi^-$ decay amplitude model parameters are summarized in Table III. The data distributions are shown in Figs. 4 and 6, and projections of the fit are shown in Fig. 6. The fit reproduces the data distributions well over the full range of the Dalitz plot. The fit projections exhibit a few deviations, e.g., for the $\rho(770)^0$–$\omega(782)$ interference region in the $M^2_{\pi^+\pi^-}$ projection; these are very small compared to the overall scale of agreement.

The quality of the fit is estimated by a two-dimensional χ^2 test. The Dalitz plot data distributions are binned into square intervals with an edge length of 0.01 GeV/c^2 and then compared to the fit function. A reduced χ^2 of 1.05 is obtained for 31272 d.o.f. based on statistical uncertainties only, a good fit quality compared to previous models of this decay [54,55,57,65,66]. The normalized residuals contributing to the χ^2 function vary approximately uniformly over the Dalitz plot phase space and do not exhibit any macroscopic deviations or structures.

The fit fractions (FFs) are evaluated to quantify the contributions of individual amplitudes. The FF for the rth intermediate resonant or nonresonant contribution is defined as

$$FF_r = \frac{a_r^2 \int_D |\mathcal{A}_r(M^2_{K^0_S\pi^-}, M^2_{K^0_S\pi^+})|^2 dM^2_{K^0_S\pi^-} dM^2_{K^0_S\pi^+}}{\int_D |\mathcal{A}(M^2_{K^0_S\pi^-}, M^2_{K^0_S\pi^+})|^2 dM^2_{K^0_S\pi^-} dM^2_{K^0_S\pi^+}}. \quad (21)$$

The fit fractions do not necessarily sum to unity, due to possible constructive or destructive interference effects among the amplitudes. In the present Dalitz plot amplitude analysis, the total fit fraction is 101.6%. The $D^0 \to K^0_S\pi^+\pi^-$ decay is dominated by the $D^0 \to K^*(892)^-\pi^+$ mode which has a fit fraction of 59.9%. The second largest contribution is $D^0 \to K^0_S\rho(770)^0$ with a fit fraction of 20.4%, followed by the $\pi^+\pi^-S$-wave with 10.0%.

To further test the agreement of the Dalitz plot amplitude model with the data, we follow an approach employed by *BABAR* in Ref. [67]. The Dalitz plot data distributions along the mass-squared directions are weighted by $Y^0_k(\cos\theta) = \sqrt{(2k+1)/4\pi}P_k(\cos\theta)$, where P_k is the Legendre polynomial function of kth-order, and compared to the expectation of the corresponding Legendre moment computed from the Dalitz plot amplitude model. For $M^2_{K^0_S\pi^-}$ and $M^2_{\pi^+\pi^-}$, the weighted data distributions and the Legendre moments up to the third-order are shown in Fig. 7. The chosen representation is sensitive to the local phase and interference structures of the contributing amplitudes and is complementary to the mass-squared projections. We find good agreement between the data distributions and the Dalitz plot amplitude model.

The chosen parametrization and composition of the $D^0 \to K^0_S\pi^+\pi^-$ decay amplitude model is very similar to those in previous measurements performed by *BABAR* [57] and Belle [55]. All measurements combine the isobar ansatz to parametrize the P- and D-wave quasi-two-body amplitudes with the K-matrix approach and the LASS parametrization to describe the $\pi\pi$ and $K\pi$ S-wave contributions, respectively. There are, however, small differences in the compositions of the models. The previous Belle analysis includes the doubly Cabibbo-suppressed $K^*(1680)^+\pi^-$ resonance, while *BABAR* and the present measurement do not. The previous Belle analysis and the present model include the $K^0_S\rho(1450)^0$, $K^*(1410)^-\pi^+$, and $K^*(1410)^+\pi^-$, while *BABAR* does not. These resonances have very small contributions with FFs at the subpercent level. Overall, the FFs agree well for the resonant and nonresonant contributions common in the model of the present measurement and those of *BABAR* and Belle.

TABLE III. Results for the amplitude magnitudes a_r, phases ϕ_r, fit fractions, K-matrix parameters for the $\pi^+\pi^-$ S-wave, LASS parameters for the $K\pi$ S-wave, and $K^*(892)^\pm$ parameters determined by the $D^0 \to K^0_S\pi^+\pi^-$ Dalitz plot fit performed for $D^{*+} \to D^0\pi^+_s$ events reconstructed from Belle data. Uncertainties are statistical only. The fit fractions are derived from the fitted parameters of the model and are quoted as central values only as the evaluation of their uncertainties would be computationally expensive.

Resonance	Amplitude	Phase (deg)	Fit fraction (%)
$K^0_S\rho(770)^0$	1 (fixed)	0 (fixed)	20.4
$K^0_S\omega(782)$	0.0388 ± 0.0005	120.7 ± 0.7	0.5
$K^0_S f_2(1270)$	1.43 ± 0.03	-36.3 ± 1.1	0.8
$K^0_S\rho(1450)^0$	2.85 ± 0.10	102.1 ± 1.9	0.6
$K^*(892)^-\pi^+$	1.720 ± 0.006	136.8 ± 0.2	59.9
$K^*_2(1430)^-\pi^+$	1.27 ± 0.02	-44.1 ± 0.8	1.3
$K^*(1680)^-\pi^+$	3.31 ± 0.20	-118.2 ± 3.1	0.5
$K^*(1410)^-\pi^+$	0.29 ± 0.03	99.4 ± 5.5	0.1
$K^*(892)^+\pi^-$	0.164 ± 0.003	-42.2 ± 0.9	0.6
$K^*_2(1430)^+\pi^-$	0.10 ± 0.01	-89.6 ± 7.6	<0.1
$K^*(1410)^+\pi^-$	0.21 ± 0.02	150.2 ± 5.3	<0.1
$\pi^+\pi^-$ S-wave parameters			10.0
β_1	8.5 ± 0.5	68.5 ± 3.4	
β_2	12.2 ± 0.3	24.0 ± 1.4	
β_3	29.2 ± 1.6	-0.1 ± 2.5	
β_4	10.8 ± 0.5	-51.9 ± 2.4	
$f^{\rm prod}_{11}$	8.0 ± 0.4	-126.0 ± 2.5	
$f^{\rm prod}_{12}$	26.3 ± 1.6	-152.3 ± 3.0	
$f^{\rm prod}_{13}$	33.0 ± 1.8	-93.2 ± 3.1	
$f^{\rm prod}_{14}$	26.2 ± 1.3	-121.4 ± 2.7	
$s^{\rm prod}_0$	-0.07 (fixed)		
$K\pi$ S-wave parameters			
$K^*_0(1430)^-\pi^+$	2.36 ± 0.06	99.4 ± 1.7	7.0
$K^*_0(1430)^+\pi^-$	0.11 ± 0.01	162.3 ± 6.6	<0.1
$M_{K^*_0(1430)^\pm}(\mathrm{GeV}/c^2)$	1.441 ± 0.002		
$\Gamma_{K^*_0(1430)^\pm}(\mathrm{GeV})$	0.193 ± 0.004		
F	$+0.96 \pm 0.07$		
R	1 (fixed)		
a	$+0.113 \pm 0.006$		
r	-33.8 ± 1.8		
$\phi_F(\mathrm{deg})$	0.1 ± 0.3		
$\phi_R(\mathrm{deg})$	-109.7 ± 2.6		
$K^*(892)^\pm$ parameters			
$M_{K^*(892)^\pm}(\mathrm{GeV}/c^2)$	0.8937 ± 0.0001		
$\Gamma_{K^*(892)^\pm}(\mathrm{GeV})$	0.0472 ± 0.0001		

6. Model variations and cross-checks

The Dalitz plot amplitude analysis of $D^0 \to K^0_S\pi^+\pi^-$ decays is validated by various cross-checks. Before choosing the nominal Dalitz plot amplitude model, several alternative parametrizations and model variations were considered.

The addition of further resonances [e.g., the $K^*(1680)^+\pi^-$ mode] does not improve the fit quality nor yield significant fit fractions for these additional resonances. Parametrizing the $\rho(770)^0$ resonance by the Gounaris-Sakurai line-shape function [68] instead of the BW line-shape provides worse agreement with data in

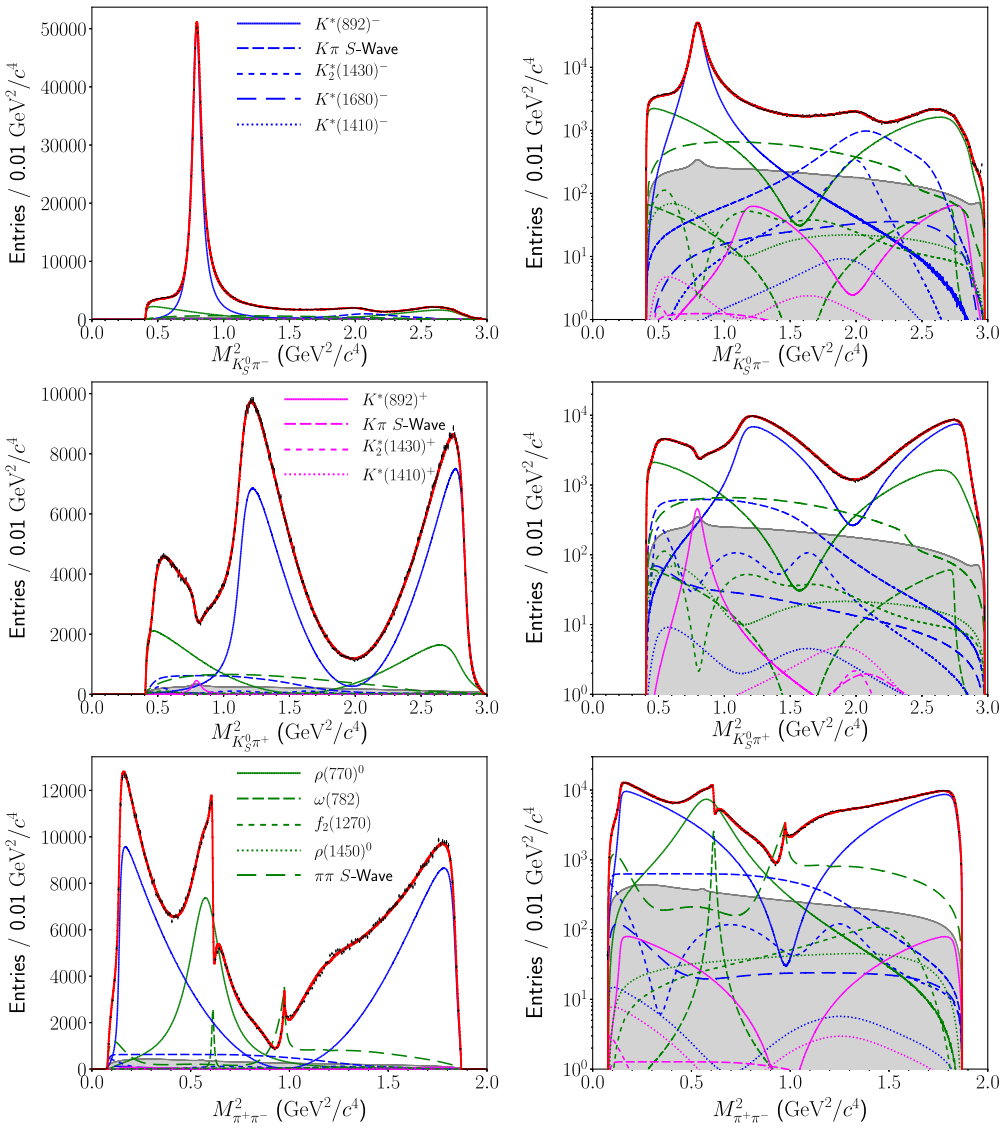

FIG. 6. Projections of the Dalitz plot data distributions (points with error bars) for $D^0 \to K^0_S\pi^+\pi^-$ from $D^{*+} \to D^0\pi^+_s$ decays reconstructed from Belle $e^+e^- \to c\bar{c}$ data, and of the result of the fit (lines). The red solid lines show the projections of the total fit function including background. The dotted and dashed colored lines show projections of the individual components of the $D^0 \to K^0_S\pi^+\pi^-$ decay amplitude model. The blue, magenta, and green lines represent resonant and nonresonant contributions originating from the $M^2_{K^0_S\pi^-}$, $M^2_{K^0_S\pi^+}$, and $M^2_{\pi^+\pi^-}$ systems, respectively. The left plots use a linear scale on the y-axis. The right plots show the same data distributions and fit projections with a log-scale in order to increase the visibility of components with very low fit fractions, and other details of the model. The components are computed from the squared amplitude of each intermediate resonant and nonresonant contribution, scaled by its fit fraction. Several quantum mechanical phenomena can be observed: for example, the complex constructive and destructive interference patterns, and the dynamic generation of the peak by the K-matrix formalism located close to the $f_0(980)$ in the $M^2_{\pi^+\pi^-}$ spectrum.

the $\rho(770)^0$ and the $\rho(770)^0$–$\omega(782)$ interference region. The addition of further parameters in the Dalitz plot fit [e.g., the mass and the width of the $\rho(770)^0$, $\omega(782)$, or other resonances] does not significantly improve the fit quality. We therefore fix these parameters to their world averages [45] in our nominal model, in order to reduce the complexity of the Dalitz plot fit.

The inclusion of a term constant in phase space to the baseline model to account for possible additional direct nonresonant three-body decays results in negligibly small fit fractions for this component.

Instead of using the K-matrix and the LASS parametrization to describe the $\pi^+\pi^-$ and $K\pi$ S-waves, a model based on a pure isobar approach has been considered. In the

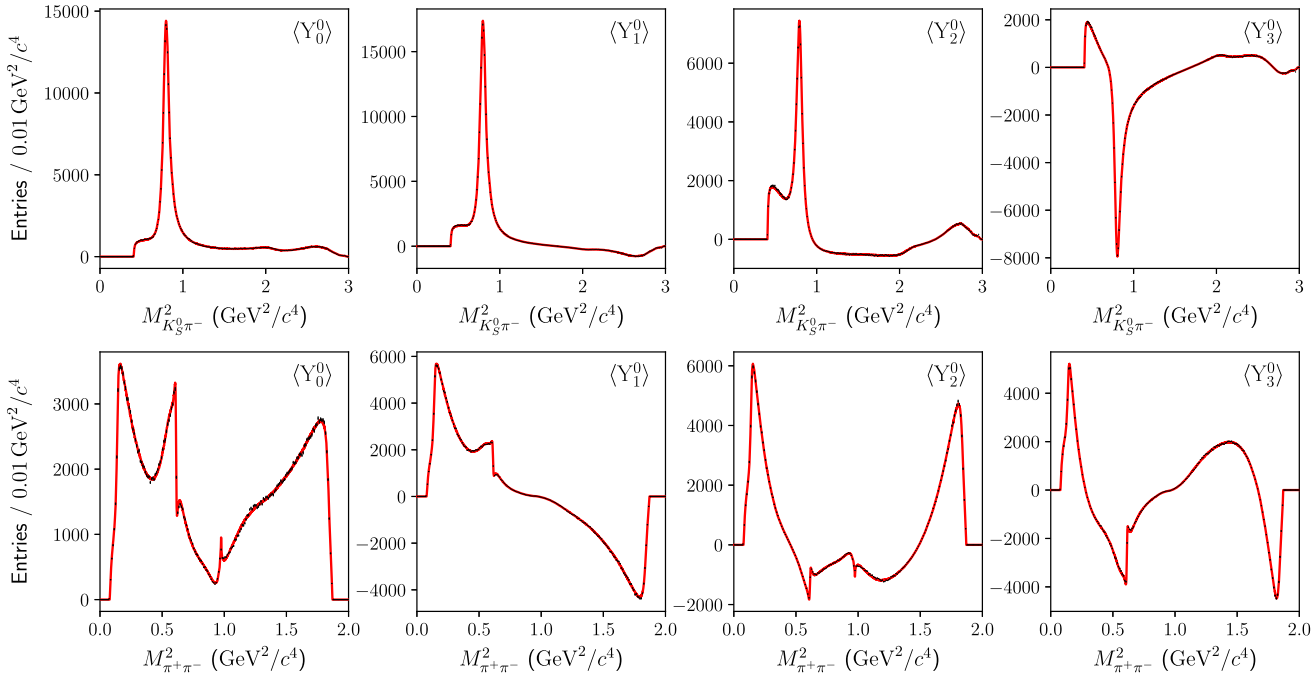

FIG. 7. Dalitz plot data distributions (points with error bars) for $D^0 \to K^0_S\pi^+\pi^-$ from $D^{*+} \to D^0\pi^+_s$ decays reconstructed from Belle $e^+e^- \to c\bar{c}$ data, and projections of the Dalitz plot fit (red solid lines) for $M^2_{K^0_S\pi^-}$ (top) and $M^2_{\pi^+\pi^-}$ (bottom) weighted by the corresponding Legendre moments.

isobar model, the $\pi^+\pi^-$ S-wave is modeled by the σ_1, σ_2, $f_0(980)$, and $f_0(1370)$ resonances, and the $K\pi$ S-waves by the Cabibbo-favored $K^*_0(1430)^-$ and the doubly Cabibbo-suppressed $K^*(1410)^+$ resonances parametrized by BW line-shapes. An additional term constant in phase space is added to account for nonresonant contributions. For the isobar model, a reduced χ^2 of 1.23 is obtained for 31287 d.o.f. A similar isobar model including the σ_2 resonance has been used before by Belle [65,69] and CDF [66] in Dalitz plot amplitude analyses of $D^0 \to K^0_S\pi^+\pi^-$ decays. However, since the physical nature for all these states is not firmly established, in particular for the σ_2 resonance, and worse agreement with the data was observed for the isobar model, it is not chosen as the nominal model.

The CLEO experiment made a model-independent determination of the relative strong phase between D^0 and $\bar{D}^0 \to K^0_S\pi^+\pi^-$ decays by exploiting the quantum correlation of $D^0\bar{D}^0$ pairs produced from $\psi(3770)$ decays in e^+e^- annihilations [70]. The results obtained in eight bins of the Dalitz phase space are compared to the relative strong phase evaluated from the nominal Dalitz plot amplitude model, leading to very good agreement, a p-value of 0.46, with the model-independent measurement. The results also agree well with a previous *BABAR* model of the same decay [57] that has been applied by CLEO to optimize the binning for the model-independent measurement of the relative strong phase.

IV. TIME-DEPENDENT DALITZ PLOT ANALYSIS OF $B^0 \to D^{(*)}h^0$ WITH $D \to K^0_S\pi^+\pi^-$ DECAYS USING *BABAR* AND BELLE DATA

A. Event reconstruction and selection

The performance of the *BABAR* and Belle detectors is similar, allowing the use of nearly identical selection requirements in the joint analysis. The event reconstruction and applied selection requirements discussed below follow the strategy used for the previous combined *BABAR*+Belle analysis of $B^0 \to D^{(*)}_{CP}h^0$ decays described in Ref. [31].

Charged pion candidates are formed from tracks that are reconstructed from hits in the tracking detectors that meet charged particle quality criteria [36,37]. Photons are reconstructed from energy deposits of electromagnetic showers detected in the electromagnetic calorimeters. The energy of a photon candidate is required to be at least 30 MeV.

Neutral pions are reconstructed by combining two photon candidates. The invariant mass of a π^0 meson candidate is required to be within $[-20, +15]$ MeV$/c^2$ of the nominal π^0 mass [45]. The η mesons are reconstructed in the decay modes $\eta \to \gamma\gamma$ and $\pi^+\pi^-\pi^0$. The invariant mass is required to be within $[-25, +20]$ MeV$/c^2$ and ± 10 MeV$/c^2$ of the nominal η mass [45] for $\eta \to \gamma\gamma$ and $\eta \to \pi^+\pi^-\pi^0$ candidates, respectively. The ω mesons are reconstructed in the decay mode $\omega \to \pi^+\pi^-\pi^0$. The invariant mass of an ω meson candidate is required to be within $[-15, +10]$ MeV$/c^2$ of the nominal ω mass [45].

Neutral kaons are reconstructed in the decay mode $K^0_S \to \pi^+\pi^-$. The invariant mass of a K^0_S meson candidate is required to be within ± 15 MeV$/c^2$ of the nominal value [45]. Standard selection requirements exploiting the displacement of the K^0_S decay vertex from the e^+e^- interaction point (IP) described in Refs. [46,71] are applied.

Neutral D mesons are reconstructed in the decay mode $D \to K^0_S\pi^+\pi^-$. The invariant mass of a D meson candidate is required to be within ± 15 MeV$/c^2$ of the nominal value [45]. Neutral D^* mesons are reconstructed in the decay mode $D^* \to D\pi^0$. To select D^* mesons, the reconstructed mass difference of neutral D^* and D meson candidates is required to be within ± 2.5 MeV$/c^2$ of the nominal value [45].

Neutral B mesons are reconstructed by combining light unflavored and neutral hadron candidates, $h^0 \in \{\pi^0, \eta, \omega\}$, with $D^{(*)}$ candidates. The decay modes $B^0 \to D\pi^0$, $D\eta$, $D\omega$, $D^*\pi^0$, and $D^*\eta$, where sufficient signal yields are reconstructed, are included in the analysis. Neutral B mesons are selected using three variables constructed from kinematic observables: the beam-energy-constrained mass $M'_{\rm bc}$, the energy difference ΔE, and the neural network classifier $\mathcal{C}'_{NN_{\rm out}}$.

The beam-energy-constrained mass is defined as

$$M'_{\rm bc} = \sqrt{E^{*2}_{\rm beam}/c^4 - \left(\vec{p}^{\,*}_{D^{(*)}}/c + \frac{\vec{p}^{\,*}_{h^0}}{|\vec{p}^{\,*}_{h^0}|}\sqrt{(E^*_{\rm beam} - E^*_{D^{(*)}})^2/c^4 - M^2_{h^0}}\right)^2}, \tag{22}$$

where $E^*_{\rm beam}$ is the energy of either beam provided by the e^+e^- collider; the variables $\vec{p}^{\,*}_{D^{(*)}}$ and $E^*_{D^{(*)}}$ are the three-momentum and the energy of the $D^{(*)}$ meson candidates, respectively; and $\vec{p}^{\,*}_{h^0}$ and M_{h^0} are the three-momentum and the invariant mass of the h^0 candidates, respectively. Observables marked with an asterisk are evaluated in the e^+e^- c.m. frame. Belle introduced the variable $M'_{\rm bc}$ in the measurements of B meson decays mediated by radiative penguin transitions [72] as an alternative to the more commonly used variable $M_{\rm bc} = \sqrt{E^{*2}_{\rm beam}/c^4 - \vec{p}^{\,*2}_B/c^2} = \sqrt{E^{*2}_{\rm beam}/c^4 - (\vec{p}^{\,*}_{D^{(*)}} + \vec{p}^{\,*}_{h^0})^2/c^2}$. We note that $M'_{\rm bc}$ does not directly depend on the three-momentum magnitude nor the energy, but only on the direction of flight of the h^0 candidate. Therefore, $M'_{\rm bc}$ is insensitive to potential correlations with the energy difference, defined as

$$\Delta E = E^*_B - E^*_{\rm beam}. \tag{23}$$

In this analysis, nontrivial correlations emerge between $M_{\rm bc}$ and ΔE for final states containing photons from the reconstructed h^0 decay modes due to energy mismeasurements by the electromagnetic calorimeters, e.g., caused by shower leakage effects. The use of $M'_{\rm bc}$ in multi-dimensional fits effectively eliminates these correlations and enables factorizing the p.d.f.s constructed from the $M'_{\rm bc}$ and ΔE observables.

The neural network combines information characterizing the shape of the events and is based on 16 modified Fox-Wolfram moments [73,74]. Following an approach introduced by Belle in Ref. [75], the variable $\mathcal{C}'_{NN_{\rm out}}$ is constructed from the output of the neural network classifier, $\mathcal{C}_{NN_{\rm out}}$, by the following transformation:

$$\mathcal{C}'_{NN_{\rm out}} = \log\frac{\mathcal{C}_{NN_{\rm out}} - \mathcal{C}^{\rm min}_{NN_{\rm out}}}{\mathcal{C}^{\rm max}_{NN_{\rm out}} - \mathcal{C}_{NN_{\rm out}}}. \tag{24}$$

The variables $\mathcal{C}^{\rm min}_{NN_{\rm out}}$ and $\mathcal{C}^{\rm max}_{NN_{\rm out}}$ are adjustable parameters related to the output domain of $\mathcal{C}_{NN_{\rm out}}$. In this analysis, $\mathcal{C}^{\rm min}_{NN_{\rm out}} = 0.2$ and $\mathcal{C}^{\rm max}_{NN_{\rm out}} = 1$ are chosen. After the transformation to $\mathcal{C}'_{NN_{\rm out}}$, the output of the neural network classifier exhibits smooth distributions around a peak position that differs for $e^+e^- \to q\bar{q}$ $(q \in \{u, d, s, c\})$ continuum events and $B\bar{B}$ events. Candidates from continuum events tend to be distributed around a peak position at negative values of $\mathcal{C}'_{NN_{\rm out}}$, while $B\bar{B}$ events are distributed around a peak position at positive values. The $\mathcal{C}'_{NN_{\rm out}}$ distributions can be described by empirical parametrized models with few d.o.f., such as the Novosibirsk function, an empirical p.d.f. inspired by the log-normal distribution and defined in Ref. [76]. The use of a parametrized model has technical advantages when including the neural network classifier in multi-dimensional fits along with $M'_{\rm bc}$ and ΔE to extract the $B^0 \to D^{(*)}h^0$ signal. Before applying the transformation described above, a loose requirement of $\mathcal{C}_{NN_{\rm out}} > 0.2$ is applied to remove regions that are almost exclusively populated by continuum background events.

The following requirements are made on $M'_{\rm bc}$, ΔE, and $\mathcal{C}'_{NN_{\rm out}}$ to select neutral B mesons: $5.24 < M'_{\rm bc} < 5.29\,{\rm GeV}/c^2$, $-150 < \Delta E < 200$ MeV, and $-8 < \mathcal{C}'_{NN_{\rm out}} < 10$.

B. Estimation of the $B^0 \to D^{(*)}h^0$ signal yields

The $B^0 \to D^{(*)}h^0$ signal yields are determined by three-dimensional extended unbinned ML fits to the $M'_{\rm bc}$, ΔE, and $\mathcal{C}'_{NN_{\rm out}}$ distributions. The fit model accounts for five components and is described below.

For $B^0 \to D^{(*)}h^0$ signal decays, the $M'_{\rm bc}$, ΔE, and $\mathcal{C}'_{NN_{\rm out}}$ distributions exhibit smooth peaking structures. The shapes of the signal component are parametrized by two Novosibirsk functions for $M'_{\rm bc}$, one symmetric and two two-piece normal distributions for ΔE, and two Novosibirsk functions for $\mathcal{C}'_{NN_{\rm out}}$. The signal shapes are calibrated using the high-statistics data control sample of $B^0 \to \bar{D}^{(*)0}h^0$ decays with the CKM-favored $\bar{D}^0 \to K^+\pi^-$ decay.

For $B^0 \to Dh^0$ decays, candidates can originate from the corresponding $B^0 \to D^*h^0$ decay modes, if the slow neutral pion from $D^* \to D\pi^0$ decays is missed during the reconstruction. This "cross-feed component" originates from true $B^0 \to D^*h^0$ signal decays and thus has signal-like properties. The cross-feed has similar shapes as the signal but peaks at negative ΔE. The contribution of the cross-feed is small, at the level of 3%–13% with respect to the signal. In the fits, the fractions of this component are fixed to the values estimated from high-statistics MC simulations of signal decays. The shapes of the cross-feed component are parametrized by two Novosibirsk functions for $M'_{\rm bc}$, one kernel density estimator for ΔE, and two Novosibirsk functions for $\mathcal{C}'_{NN_{\rm out}}$.

In addition to the contributions from the signal and the signal-like cross-feed, the fit model accounts for the following three separate sources of background. The first source originates from partially reconstructed $B^+ \to \bar{D}^{(*)0}\rho^+$ decays, which constitute a background for $B^0 \to D^{(*)}\pi^0$ decays when the charged pion from $\rho^+ \to \pi^+\pi^0$ decays is soft. This background arises only for $B^0 \to D\pi^0$ and $B^0 \to D^*\pi^0$ decays, but is not present for the other $B^0 \to D^{(*)}h^0$ decay modes. Like the cross-feed component, the background from $B^+ \to \bar{D}^{(*)0}\rho^+$ decays has a shape similar to that of the signal, but peaks at negative ΔE. The shapes are parametrized by two Novosibirsk functions for $M'_{\rm bc}$, one kernel density estimator for ΔE, and two Novosibirsk functions for $\mathcal{C}'_{NN_{\rm out}}$. The $B^+ \to \bar{D}^{(*)0}\rho^+$ background component is determined by the fit.

There is a small "combinatorial $B\bar{B}$ background" arising from B meson candidates formed from random combinations of final state particles originating from $e^+e^- \to B\bar{B}$ events. The background has a smooth phase space distribution in $M'_{\rm bc}$ and ΔE, and peaks at positive $\mathcal{C}'_{NN_{\rm out}}$. The shapes are parametrized by an ARGUS function [77] for $M'_{\rm bc}$, a second-order polynomial function for ΔE, and two Novosibirsk functions for $\mathcal{C}'_{NN_{\rm out}}$.

The third source of background originates from $e^+e^- \to q\bar{q}$ $(q \in \{u, d, s, c\})$ continuum events. This continuum background also has a smooth phase space distribution in $M'_{\rm bc}$ and ΔE, and peaks at negative $\mathcal{C}'_{NN_{\rm out}}$. The shapes are parametrized by an ARGUS function for $M'_{\rm bc}$, a second-order polynomial function for ΔE, and two Novosibirsk functions for $\mathcal{C}'_{NN_{\rm out}}$.

TABLE IV. Summary of the $B^0 \to D^{(*)}h^0$ signal yields determined by the three-dimensional extended unbinned ML fits to the $M'_{\rm bc}$, ΔE, and $\mathcal{C}'_{NN_{\rm out}}$ distributions described in Sec. IV B.

Decay mode	*BABAR*	Belle
$B^0 \to D\pi^0$	469 ± 31	768 ± 37
$B^0 \to D\eta$	220 ± 22	238 ± 23
$B^0 \to D\omega$	219 ± 21	285 ± 26
$B^0 \to D^*\pi^0$	147 ± 18	182 ± 19
$B^0 \to D^*\eta$	74 ± 11	94 ± 13
Total	$1\,129 \pm 48$	$1\,567 \pm 56$

In total, we obtain $B^0 \to D^{(*)}h^0$ signal yields of 1129 ± 48 events for *BABAR* and 1567 ± 56 events for Belle. The signal yields, separated by experiment and decay mode, are summarized in Table IV. The experimental $M'_{\rm bc}$, ΔE, and $\mathcal{C}'_{NN_{\rm out}}$ distributions and projections of the fits are shown in Fig. 8.

C. Time-dependent Dalitz plot analysis

At *BABAR* (Belle) the $\Upsilon(4S)$ is produced with a Lorentz boost of $\beta\gamma = 0.560$ (0.425), allowing the measurement of the proper-time interval between the decays of the two B mesons. The proper-time interval Δt is given by $\Delta z/c\beta\gamma$, where Δz denotes the spatial distance between the decay vertices of the two B mesons in the laboratory frame. The *BABAR* and Belle techniques to measure the flavor-tagged proper-time intervals of the B mesons and to extract the CP violation parameters are described in detail in Refs. [14–16,78–81]. The $B^0 \to D^{(*)}h^0$ signal decay vertices are reconstructed by kinematic fits that include experimental knowledge of the IP position. For *BABAR*, the applied vertex reconstruction algorithm simultaneously includes the complete B meson decay tree, including all secondary decays, in the kinematic fit. For Belle, the vertex reconstruction is performed in an iterative bottom-up approach starting with the final state particles. The decay vertex and the b-flavor content of the accompanying B meson are estimated from the reconstructed decay products not assigned to the signal B meson. The b-flavor content is inferred by the flavor-tagging procedures described in Refs. [15,80]. The applied algorithms assign a flavor and an associated probability, accounting for different signatures, such as the presence and properties of prompt leptons, charged kaons, and pions originating from the decay of the accompanying B meson.

The experimental conditions and the instrumentation of the detectors are different for *BABAR* and Belle. These produce different experimental resolutions in the measurements of proper-time intervals, and both experiments follow different approaches to describe the resolution effects. The two experiments employ different multivariate techniques for the flavor-tagging. *BABAR* uses a neural-network-based approach while Belle uses a multi-dimensional likelihood approach.

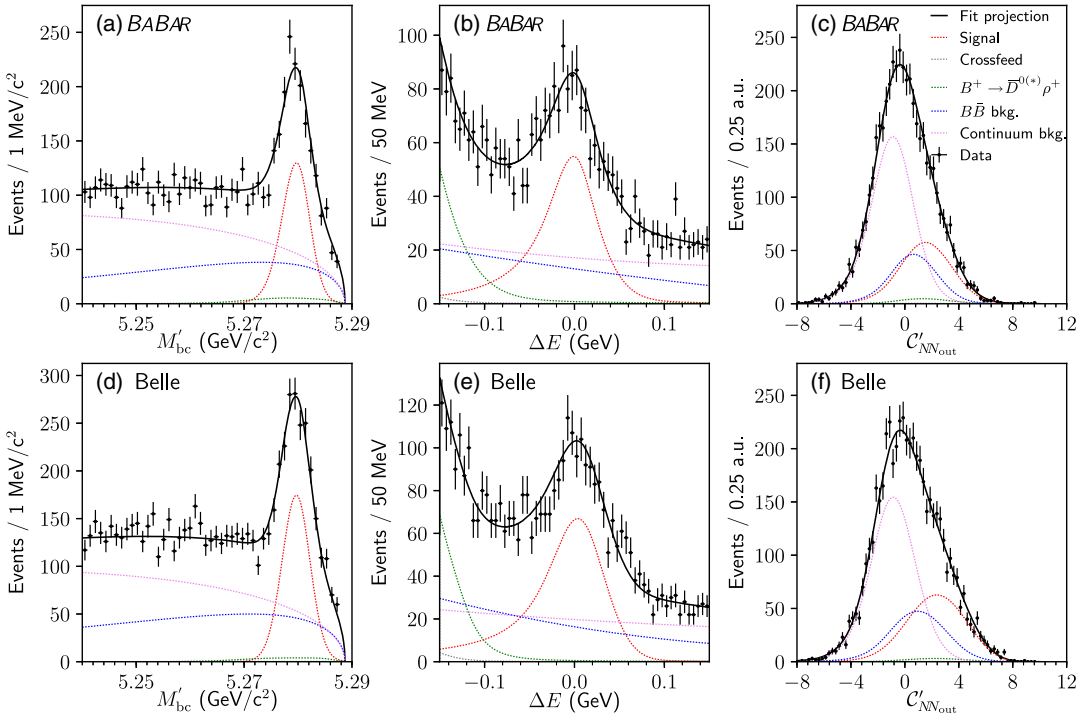

FIG. 8. Data distributions for $M'_{\rm bc}$ (left), ΔE (center), and $\mathcal{C}'_{NN_{\rm out}}$ (right) for $B^0 \to D^{(*)}h^0$ decays (points with error bars) reconstructed from *BABAR* (top) and Belle (bottom) data. The solid black lines represent projections of the total fit function, and the colored dotted lines show the signal and background components of the fit as indicated in the legend of the upper right panel. In plotting the $M'_{\rm bc}$, ΔE, and $\mathcal{C}'_{NN_{\rm out}}$ distributions, each of the other two observables are required to satisfy $M'_{\rm bc} > 5.272$ GeV/c^2, $|\Delta E| < 100$ MeV, or $0 < \mathcal{C}'_{NN_{\rm out}} < 8$ to select signal-enhanced regions.

The time-dependent Dalitz plot analysis to measure the CP violation parameters follows the technique established in the previous combined *BABAR*+Belle time-dependent CP violation measurement of $\bar{B}^0 \to D^{(*)}_{CP}h^0$ decays [31]. The strategy of the combined approach is to apply established experiment-specific techniques to describe proper-time resolution and flavor-tagging effects by *BABAR* and Belle to the data collected by the particular experiment. The combined measurement is then performed by maximizing the log-likelihood function constructed from the p.d.f.s and the data collected by both experiments:

$$\ln \mathcal{L} = \sum_i \ln \mathcal{P}_i^{BABAR} + \sum_j \ln \mathcal{P}_j^{\rm Belle}. \qquad (25)$$

The indices i and j run over events reconstructed from *BABAR* and Belle data, respectively. All events used in the $M'_{\rm bc}$, ΔE, and $\mathcal{C}'_{NN_{\rm out}}$ fits are included. The $\mathcal{P}$ are the p.d.f.s of the experimental flavor-tagged proper-time interval and Dalitz plot distributions of the B mesons measured in the events, and they are defined as

$$\mathcal{P} = \sum_k f_k \int [P_k(\Delta t')R_k(\Delta t - \Delta t')]d(\Delta t'). \qquad (26)$$

The index k represents the signal and background components. The fractions of the components, f_k, are evaluated on an event-by-event basis as a function of $M'_{\rm bc}$, ΔE, and $\mathcal{C}'_{NN_{\rm out}}$. The P_k are the p.d.f.s that describe the particular underlying particle physics process and are the same for both experiments. The P_k are convolved with the resolution functions R_k that account for the finite proper-time resolution.

For the signal, the p.d.f.s are constructed from Eqs. (1) and (2) convolved with the experiment-specific resolution functions to account for the finite proper-time resolution [15,79]. They include the effect of incorrect flavor assignments by the applied flavor-tagging algorithms [15,80] and a correction to account for the variations of the reconstruction efficiency as a function of the position on the Dalitz plot.

Neutral D mesons produced in $B^0 \to D^{(*)}h^0$ decays have a different momentum spectrum than those produced in $e^+e^- \to c\bar{c}$ events. In addition, the yield for the $B^0 \to D^{(*)}h^0$ decay modes studied by the combined *BABAR*+Belle approach is about three orders of magnitude lower than that for the $D^0 \to K^0_S\pi^+\pi^-$ decays reconstructed from $e^+e^- \to c\bar{c}$ events. Therefore, the Dalitz plot reconstruction efficiency correction used for the analysis of $B^0 \to D^{(*)}h^0$ decays is different from that described in

Sec. III C 2, and a parametrization with fewer d.o.f. is chosen. The reconstruction efficiency map is constructed separately for *BABAR* and Belle by the fit of a two-dimensional third-order polynomial function in the Dalitz plot variables $M^2_{K^0_S\pi^-}$ and $M^2_{K^0_S\pi^+}$ to the reconstruction efficiency distributions obtained from high-statistics samples of MC events of $B^0 \to D^{(*)}h^0$ with $D \to K^0_S\pi^+\pi^-$ signal decays.

To account for the signal-like cross-feed from partially reconstructed $B^0 \to D^*h^0$ decays, the p.d.f.s are constructed as for the signal, but account for distinct properties such as the CP eigenvalues of the particular final states of the cross-feed contribution. The charged B meson background from partially reconstructed $B^+ \to \bar{D}^{(*)0}\rho^+$ decays is parametrized by an exponential p.d.f. accounting for the B^+ lifetime convolved with the experiment-specific resolution functions. The combinatorial $B\bar{B}$ background and the continuum background share the same parametrization for *BABAR* and Belle. For each background component, the p.d.f.s are constructed from the sum of a Dirac delta function to model background from prompt particles and an exponential p.d.f.s with effective lifetimes to model the non-prompt background. The background p.d.f.s are convolved with a resolution function modeled as the sum of two Gaussian functions whose widths depend linearly on the uncertainty of Δt. The Δt parameters for the combinatorial $B\bar{B}$ background and the continuum background are determined by fits to the $M'_{\rm bc} < 5.26\ {\rm GeV}/c^2$ sidebands and are fixed in the measurement.

In the fit, the parameters τ_{B^0}, τ_{B^+}, and Δm_d are fixed to the world averages [17], and the Dalitz plot amplitude model parameters are fixed to the results of the $D^0 \to K^0_S\pi^+\pi^-$ Dalitz plot fit described above. The only free parameters, $\sin 2\beta$ and $\cos 2\beta$, are determined to be

$$\begin{aligned}\sin 2\beta &= 0.80 \pm 0.14({\rm stat}) \pm 0.06({\rm syst}) \pm 0.03({\rm model}),\\ \cos 2\beta &= 0.91 \pm 0.22({\rm stat}) \pm 0.09({\rm syst}) \pm 0.07({\rm model}).\end{aligned} \tag{27}$$

The linear correlation between $\sin 2\beta$ and $\cos 2\beta$ is 5.1%; the result deviates by less than 1.0 standard deviation from the trigonometric constraint $\sin^2 2\beta + \cos^2 2\beta = 1$.

A separate fit is performed to directly measure the CP-violating phase β. The measurement is performed by constructing the signal p.d.f. from Eq. (1) and using otherwise the same fit model as described above. The result is

$$\beta = (22.5 \pm 4.4({\rm stat}) \pm 1.2({\rm syst}) \pm 0.6({\rm model}))^\circ, \tag{28}$$

in agreement with the result in Eq. (27). The experimental systematic uncertainties and the uncertainties due to the applied $D^0 \to K^0_S\pi^+\pi^-$ decay amplitude model are evaluated separately for the measurement of $\sin 2\beta$ and $\cos 2\beta$ and for the measurement of β, and they are described in Secs. IV D 1 and IV D 2.

A rich variety of intermediate CP eigenstates and quasi-flavor-specific decays contribute to the multibody final states in $B^0 \to [K^0_S\pi^+\pi^-]^{(*)}_D h^0$ decays. These intermediate contributions involve different physics in the time evolution of the B meson decay and hence exhibit different proper-time interval distributions. In Fig. 9, the proper-time interval distributions and projections of the fit for $\sin 2\beta$ and $\cos 2\beta$ are shown for two different regions of the $D^0 \to K^0_S\pi^+\pi^-$ phase space.

In Figs. 9(a) and 9(c), a region of phase space predominantly populated by CP eigenstates, $B^0 \to [K^0_S\rho(770)^0]^{(*)}_D h^0$, is selected by requiring $|M_{\rho(770)} - M_{\pi^+\pi^-}| < 150\ {\rm MeV}/c^2$. Since the $[K^0_S\rho(770)^0]^{(*)}_D h^0$ final state is accessible from both B^0 and $\bar{B}^0$, interference between the amplitude for direct decays of neutral B mesons into this final state and that following B^0-$\bar{B}^0$ oscillations emerges. The time evolution exhibits time-dependent CP violation governed by the CP-violating weak phase 2β. The proper-time interval distributions show the characteristic pattern for mixing-induced CP violation, and the corresponding time-dependent CP asymmetry show a sinusoidal oscillation similar to that in our previous combined *BABAR*+Belle measurement of $\sin 2\beta$ in $\bar{B}^0 \to D^{(*)}_{CP}h^0$ decays with D_{CP} decaying into two-body CP eigenstates [31].

In Figs. 9(b) and 9(d), regions of phase space predominantly populated by quasi-flavor-specific decays, $B^0 \to [K^*(892)^\pm\pi^\mp]^{(*)}_D h^0$, are selected by requiring $|M_{K^*(892)^\pm} - M_{K^0_S\pi^\pm}| < 75\ {\rm MeV}/c^2$. The decays of neutral B mesons to the $[K^*(892)^\pm\pi^\mp]^{(*)}_D h^0$ final states are, to a good approximation, flavor specific. With no interference between B^0 and $\bar{B}^0$ mesons, there is no time-dependent CP-violating asymmetry. Instead, the time evolution exhibits B^0-$\bar{B}^0$ oscillations governed by the decay width difference of the physical eigenstates of neutral B mesons and the B^0-$\bar{B}^0$ oscillation frequency Δm_d. The proper-time interval distributions show the characteristic oscillation pattern for quantum-entangled B meson pairs produced and tagged in $e^+e^- \to \Upsilon(4S) \to B^0\bar{B}^0$ events. The Einstein-Podolsky-Rosen (EPR) effect [83] prevents the two neutral B mesons from having the same flavor at $\Delta t = 0$; this can be seen in Figs. 9(b) and 9(d) where the Δt distribution is additionally smeared by experimental effects. The time evolution follows a $1 \pm \cos(\Delta m \Delta t)$ distribution; the corresponding time-dependent oscillation asymmetry exhibits a cosine oscillation.

Cross-checks are performed to validate the measurement procedure. The $B^0 \to \bar{D}^{(*)0}h^0$ decays with the CKM-favored $\bar{D}^0 \to K^+\pi^-$ decay have very similar kinematics and background composition as $B^0 \to D^{(*)}h^0$ with $D \to K^0_S\pi^+\pi^-$ decays and thus can provide a high-statistics control sample of 3029 ± 73 events for *BABAR* and 4042 ± 84 events for Belle. Using the same analysis approach,

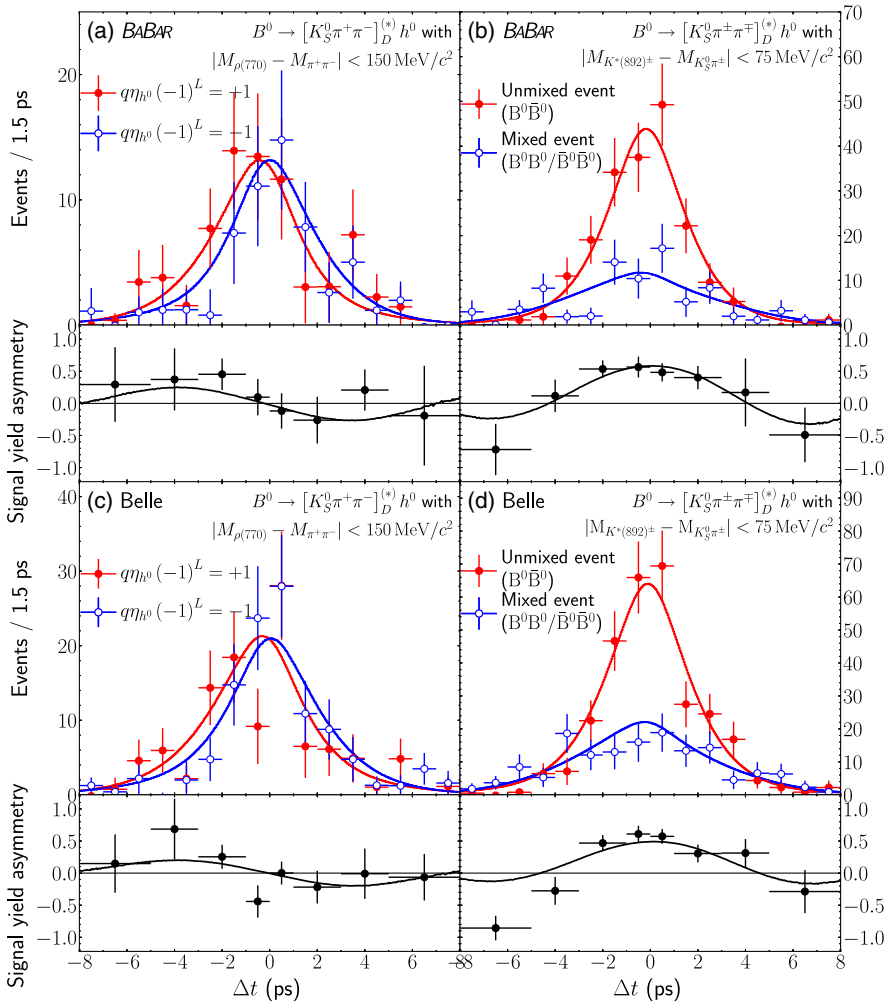

FIG. 9. Distributions of the proper-time interval (data points with error bars) and the corresponding asymmetries for $B^0 \to D^{(*)}h^0$ candidates associated with high-quality flavor-tags (*BABAR*: lepton or kaon tagging categories; Belle: $r > 0.5$) for the *BABAR* (top) and Belle (bottom) data samples. The background has been subtracted using the ${}_s\mathcal{P}lot$ technique [82] with weights obtained from the fit presented in Fig. 8. Two different regions of the $D \to K^0_S\pi^+\pi^-$ phase space are shown. In the plots of the left column, a region predominantly populated by *CP* eigenstates, $B^0 \to [K^0_S\rho(770)^0]^{(*)}_D h^0$, is selected by requiring $|M_{\rho(770)} - M_{\pi^+\pi^-}| < 150\ \mathrm{MeV}/c^2$. In the plots of the right column, a region predominantly populated by quasi-flavor-specific decays, $B^0 \to [K^*(892)^\pm\pi^\mp]^{(*)}_D h^0$, is selected by requiring $|M_{K^*(892)^\pm} - M_{K^0_S\pi^\pm}| < 75\ \mathrm{MeV}/c^2$.

the time-dependent *CP* violation measurement of the control sample yields both mixing-induced and direct *CP* violation consistent with zero, in agreement with the expectation of negligible *CP* violation for these flavor-specific decays. Measurements of the neutral B meson lifetime for $B^0 \to D^{(*)}h^0$ with $D \to K^0_S\pi^+\pi^-$ decays and for the control sample without flavor-tagging applied yield $\tau_{B^0} = (1.500 \pm 0.052(\mathrm{stat}))$ ps and $\tau_{B^0} = (1.535 \pm 0.028(\mathrm{stat}))$ ps, respectively, in agreement with the world average $\tau_{B^0} = (1.520 \pm 0.004)$ ps [17]. In addition, all measurements performed on data separated by experiment yield consistent results. The results for $B^0 \to D^{(*)}h^0$ with $D \to K^0_S\pi^+\pi^-$ decays separated by experiment are $\sin 2\beta = 0.91 \pm 0.20(\mathrm{stat})$, $\cos 2\beta = 0.87 \pm 0.31(\mathrm{stat})$, and $\beta = (25.6 \pm 6.4(\mathrm{stat}))°$ for *BABAR*, and $\sin 2\beta = 0.70 \pm 0.20(\mathrm{stat.})$, $\cos 2\beta = 0.96 \pm 0.30(\mathrm{stat})$, and $\beta = (19.6 \pm 6.1(\mathrm{stat}))°$ for Belle, respectively.

D. Determination of the systematic uncertainties

This analysis accounts for two classes of systematic uncertainties on the measured *CP* violation parameters: first, the experimental systematic uncertainty accounts for experimental effects that can affect the time-dependent Dalitz plot analysis; second, the Dalitz plot model uncertainty accounts for assumptions made on the $D^0 \to K^0_S\pi^+\pi^-$ decay amplitude model.

1. Experimental systematic uncertainties

The estimation of the experimental systematic uncertainty on the *CP* violation parameters follows established methods, described in Refs. [15,16,31]. The evaluation of the individual contributions to the experimental systematic uncertainty are described below, and the results are summarized in Table V.

The systematic uncertainty due to vertex reconstruction accounts for the applied vertex reconstruction algorithms, the requirements applied to select B mesons, the uncertainty of the z scale, possible Δt biases, and effects due to possible misalignment of the silicon vertex detectors. For the vertex reconstruction algorithms, the constraints in the kinematic fits and the applied selection requirements of the signal B meson and the accompanying B meson are varied. For *BABAR*, the uncertainty due to the z scale and the Lorentz boost is estimated by variations of the corresponding scale and uncertainties. For Belle, a possible Δt bias is estimated using MC simulations. Misalignment effects of the silicon vertex detectors are studied by MC simulations, and corresponding systematic uncertainties are assigned.

Experiment-specific resolution models are applied to account for effects due to the finite experimental Δt resolution. The Δt resolution function parameters are fixed to values obtained from control samples using *BABAR* and Belle data. The systematic uncertainty due to the applied Δt resolution functions is estimated by variation of the resolution model parameters within their uncertainties.

The parameters of the Δt model for the combinatorial $B\bar{B}$ background and the continuum background are determined by fits to the $M'_{\rm bc} < 5.26\ {\rm GeV}/c^2$ data sidebands. The systematic uncertainty due to the background Δt p.d.f.s is estimated by variation of the Δt background model parameters within their uncertainties.

The signal purity is estimated by the three-dimensional unbinned ML fit to the $M'_{\rm bc}$, ΔE, and $\mathcal{C}'_{NN_{\rm out}}$ distributions. The systematic uncertainty due to the signal purity estimation is estimated by variation of the fit parameters within their uncertainties.

The b-flavor content of neutral B mesons is inferred by multivariate *BABAR*- and Belle-specific flavor-tagging algorithms. The flavor-tagging algorithms are calibrated using control samples reconstructed from *BABAR* and Belle data. The systematic uncertainty due to the flavor-tagging is estimated by variation of the wrong-tag fractions and the corresponding wrong-tag fraction differences for each tagging category within their uncertainties.

The neutral B lifetime τ_{B^0}, the charged B meson lifetime τ_{B^+}, and the B^0-$\bar{B}^0$ oscillation frequency Δm_d are fixed to the world averages. The systematic uncertainty due to these fixed physics parameters is estimated by variation of the lifetimes and oscillation frequency within their uncertainties.

The systematic uncertainty due to a possible small fit bias in Δt measurements is estimated by MC simulations. Large MC samples are generated using a complex $D^0 \to K^0_S\pi^+\pi^-$ decay amplitude model including *CP* violation, the same reconstruction algorithms and event selection requirements are applied to the MC samples as for the data, and the time-dependent Dalitz plot analysis is performed. The deviations of the central values of the *CP* violation parameters measured using the MC samples from the nominal result are assigned as systematic uncertainties.

The effect due to the applied Dalitz plot reconstruction efficiency correction for neutral D mesons produced in $B^0 \to D^{(*)}h^0$ decays is estimated by removing the efficiency correction. The time-dependent Dalitz plot analysis is also performed without the efficiency correction, and the deviations from the nominal result are assigned as systematic uncertainty.

Most systematic uncertainties are independent for *BABAR* and Belle, and they can be treated as uncorrelated. Correlations in the evaluation of the common physics parameters are accounted for.

Additional contributions to the systematic uncertainty from possible sources of peaking background and the tag-side interference have been considered and can be neglected.

The total experimental systematic uncertainty is the quadratic sum of all these contributions.

2. Uncertainty due to the Dalitz plot amplitude model

The model uncertainty accounts for the dependence of the *CP* violation parameters on the $D^0 \to K^0_S\pi^+\pi^-$ decay amplitude model determined by the Dalitz plot amplitude analysis using the high-statistics Belle $e^+e^- \to c\bar{c}$ data

TABLE V. Experimental systematic uncertainties on the *CP* violation parameters.

Source	$\delta \sin 2\beta$ ($\times 10^2$)	$\delta \cos 2\beta$ ($\times 10^2$)	$\delta\beta$ (°)
Vertex reconstruction	3.2	4.8	0.53
Δt resolution functions	2.8	5.8	0.41
Background Δt p.d.f.s	1.2	1.8	0.16
Signal purity	2.1	3.4	0.53
Flavor-tagging	0.3	0.4	0.07
Physics parameters	0.1	0.1	0.02
Possible fit bias	3.7	3.9	0.79
Dalitz plot reconstruction efficiency correction	<0.1	0.2	0.02
Total	6.1	9.3	1.18

sample described in Sec. III C. The strategy to estimate the model uncertainty is to repeat the $D^0 \to K^0_S\pi^+\pi^-$ Dalitz plot amplitude analysis with alternative assumptions and variations of the $D^0 \to K^0_S\pi^+\pi^-$ decay amplitude model. The time-dependent Dalitz plot analysis of $B^0 \to D^{(*)}h^0$ decays is then performed using the alternative models as input, and the deviations from the result using the nominal $D^0 \to K^0_S\pi^+\pi^-$ decay amplitude model are assigned as the model uncertainty on the CP violation parameters. The evaluation of the individual contributions to the uncertainty due to the Dalitz plot amplitude model is described below; the results are summarized in Table VI.

For the masses and widths of resonances fixed to the world averages, each resonance parameter is varied within its uncertainty to estimate the associated model uncertainty.

The model uncertainty due to the chosen $\pi^+\pi^-$ S-wave parametrization using the K-matrix formalism is estimated by replacing the nominal K-matrix solution by alternative solutions from Ref. [60]. In addition, the parameter $s_0^{\rm prod}$ is varied within its uncertainty, which is taken from Ref. [57].

The LASS parametrization is used to model the $K\pi S$-waves. The model uncertainty is estimated by replacing the LASS parametrization for the $K_0^*(1430)^-$ and $K_0^*(1430)^+$ resonances by standard relativistic BW terms.

The model uncertainty due to the chosen Blatt-Weisskopf barrier factors for D mesons and intermediate resonances is estimated by varying the fixed parameters d_D and d_r each by $\pm 0.5\hbar c/\mathrm{GeV}$.

The fraction of wrong D meson flavor-tags of the flavor-tagged $c\bar{c}$ data sample is fixed to the value estimated from the fit to the ΔM sideband region on data. The D meson mistag fraction is varied within its uncertainty to evaluate the associated model uncertainty.

The model uncertainty due to the applied Dalitz plot reconstruction efficiency correction is estimated by replacing the parametrized efficiency map by the corresponding two-dimensional binned distributions.

In the Dalitz plot amplitude analysis, the background is described by a parametrized model taken from the ΔM and M_{D^0} sideband regions on data. The model uncertainty due to the applied background description is estimated by replacing the parametrized background model by the two-dimensional binned distributions from the data sidebands. Most intermediate two-body resonances contributing to $D^0 \to K^0_S\pi^+\pi^-$ decays have a natural width much larger than the finite experimental resolution of reconstructed invariant masses; resolution effects can therefore be neglected in the $D \to K^0_S\pi^+\pi^-$ Dalitz plot amplitude analysis. The $\omega(782)$ width, 8.5 MeV, is comparable to the mass resolution. To estimate the size of possible effects due to the mass resolution and to evaluate the associated model error, the width of the $\omega(782)$ is increased by 20%.

The signal and background fractions used in the Dalitz plot amplitude analysis are determined by the fit of the two-dimensional ΔM and M_{D^0} distributions. The model uncertainty due to the signal purity estimation is determined by varying the $\Delta M - M_{D^0}$ model parameters within their uncertainties.

The statistical uncertainties on the Dalitz plot amplitude model parameters that are summarized in Table III are caused by the finite size of the $c\bar{c}$ data sample. To propagate the statistical uncertainties to the CP violation parameters and assign the associated model error, each parameter is varied within its uncertainty. For individual resonances, the correlations between phases and amplitudes are accounted for. An explicit treatment of additional correlations between resonances important in the CP violation measurement found them to be negligible. This systematic uncertainty does not limit the precision of the measurement, validating the chosen approach.

The dependence of the model on resonances with very small contributions is estimated by removing resonances with fit fractions of 0.1% or lower. The doubly Cabibbo-suppressed $K^*(1410)^+$, $K_2^*(1430)^+$, and $K_0^*(1430)^+$, and the

TABLE VI. Uncertainties on the CP violation parameters due to the Dalitz plot amplitude model.

Source	$\delta \sin 2\beta$ ($\times 10^2$)	$\delta \cos 2\beta$ ($\times 10^2$)	$\delta\beta$ (°)
Masses and widths of resonances	0.7	1.7	0.13
$\pi^+\pi^-$ S-wave parametrization	1.1	1.9	0.11
$K\pi$ S-wave parametrization	1.0	1.6	0.38
Blatt-Weisskopf barrier factors	1.2	1.7	0.19
D meson mistag fraction	0.2	<0.1	0.04
Dalitz plot reconstruction efficiency	0.9	0.9	0.06
Dalitz plot background shape	<0.1	0.2	0.01
Effect of finite experimental mass resolution	0.1	0.2	<0.01
Signal purity	<0.1	<0.1	0.01
Statistical uncertainties on resonance parameters	1.6	5.0	0.37
Removal of resonances	0.6	1.3	0.09
Alternative isobar Dalitz plot model	0.7	2.8	0.08
Total	2.9	6.9	0.61

$K^*(1410)^-$ are each removed from the model. For each model variation, the $D^0 \to K^0_S\pi^+\pi^-$ Dalitz plot amplitude analysis is repeated to estimate the associated model uncertainty.

As a further cross-check and estimate of the possible model dependence, a pure isobar $D^0 \to K^0_S\pi^+\pi^-$ decay model without the K-matrix parametrization is constructed. As in the isobar model discussed in Sec. III C 6, the intermediate resonance contributions to the $\pi^+\pi^-$ S-wave are modeled by the σ_1, σ_2, $f_0(980)$, and $f_0(1370)$ resonances, and a term constant in phase space is included to account for nonresonant contributions. The $D^0 \to K^0_S\pi^+\pi^-$ Dalitz plot amplitude analysis and the time-dependent Dalitz plot analysis of $B^0 \to D^{(*)}h^0$ decays are repeated using the alternative model, and the deviations of the CP violation parameters from the baseline result are assigned as a model uncertainty. The result using the isobar model agrees well with the baseline result, indicating a small overall model dependence and validating the robustness of the measurement.

The total model uncertainty is the quadratic sum of all contributions. Overall, the uncertainty due to the Dalitz plot amplitude model is small compared to the statistical uncertainty and the experimental systematic uncertainty.

V. INTERPRETATION OF THE RESULTS

The statistical significance of the results is determined by a likelihood-ratio approach. The change in $2\ln\mathcal{L}$ is computed when the CP violation parameters are fixed to zero. The experimental systematic uncertainties and the Dalitz plot amplitude model uncertainties are included by convolution of the likelihood curves. The $-2\Delta\ln\mathcal{L}$ curves for $\sin 2\beta$, $\cos 2\beta$, and β are shown in Fig. 10. When computing $-2\Delta\ln\mathcal{L}$ values for $\sin 2\beta$ and $\cos 2\beta$, the other observable is fixed to the nominal result. Due to the low correlation between $\sin 2\beta$ and $\cos 2\beta$, this approach is effectively equivalent to profiling over the other variable. The result for $\sin 2\beta$ agrees within 0.7 standard deviations with the world average of $\sin 2\beta = 0.691 \pm 0.017$ [17] measured from $\bar{b} \to \bar{c}c\bar{s}$ transitions. The measurement excludes the hypothesis of $\cos 2\beta \le 0$ at a p-value of 2.5×10^{-4}. This corresponds to a significance of 3.7 standard deviations and thus provides the first evidence for $\cos 2\beta > 0$. The results exclude the hypothesis of $\beta = 0°$ at a p-value of 3.6×10^{-7}. This corresponds to a significance of 5.1 standard deviations and thus to an observation of CP violation in $\bar{B}^0 \to D^{(*)}h^0$ decays. The measured value for β is in very good agreement with the preferred solution of the Unitarity Triangle with the world average of $(21.9 \pm 0.7)°$ [17]. The second solution of $\pi/2 - \beta = (68.1 \pm 0.7)°$ is excluded with a p-value of 2.31×10^{-13}, corresponding to a significance of 7.3 standard deviations. Therefore, this measurement resolves a long-standing ambiguity in the determination of the parameters of the CKM Unitarity Triangle.

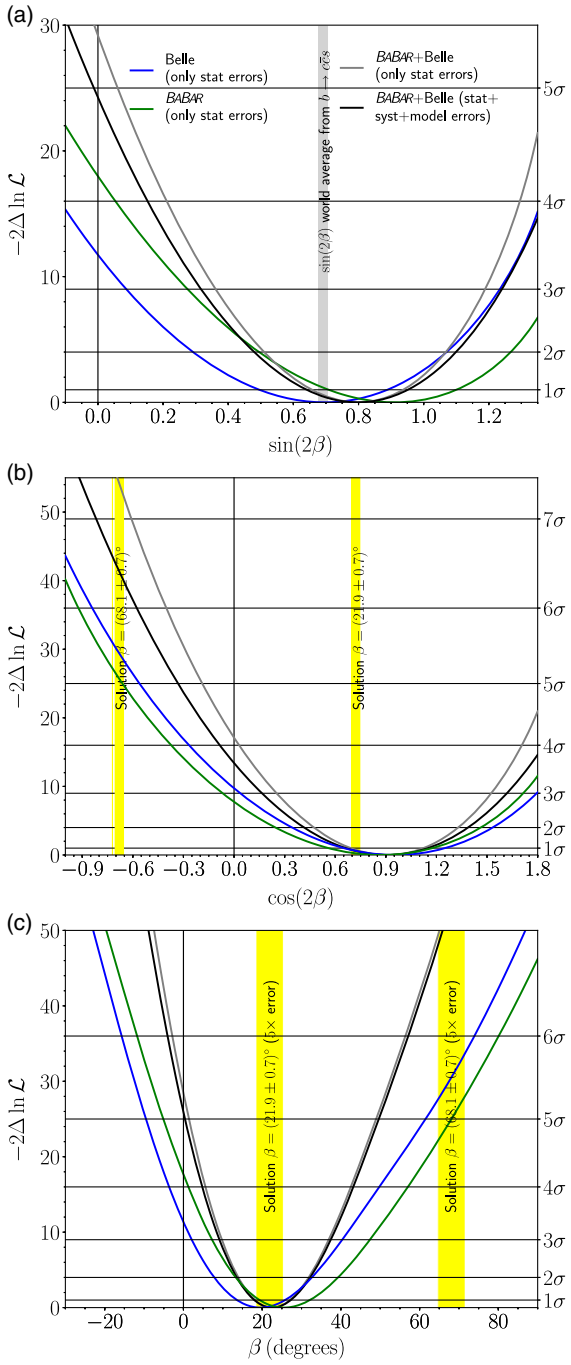

FIG. 10. Obtained $-2\Delta\ln\mathcal{L}$ curves for $\sin 2\beta$, $\cos 2\beta$, and β. The black lines represent the results of the measurement including experimental systematic uncertainties and uncertainties due to the Dalitz plot amplitude model. The green and blue lines represent the result of the measurement including only statistical uncertainties when using only *BABAR* and Belle data, respectively.

VI. CONCLUSION

In summary, we have measured $\sin 2\beta$ and $\cos 2\beta$ with a time-dependent Dalitz plot analysis of $B^0 \to D^{(*)}h^0$ with $D \to K^0_S\pi^+\pi^-$ decays. The analysis introduces new

concepts as well as several improvements over previous related measurements. First, the measurement is performed by a simultaneous analysis of the final data samples collected by the *BABAR* and Belle experiments, totaling about 1.1 ab^{-1} and containing about 1240×10^6 $B\bar{B}$ pairs collected at the $\Upsilon(4S)$ resonance. The novel combined approach enables the doubling of the statistics available for the measurement. It allows for the application of common assumptions and the same $D^0 \to K^0_S\pi^+\pi^-$ decay amplitude model simultaneously to the data collected by both experiments. Second, a full Dalitz plot amplitude analysis is performed to derive the $D^0 \to K^0_S\pi^+\pi^-$ decay amplitude model directly from a high-statistics $e^+e^- \to c\bar{c}$ data sample. This enables full control over the model-building process and the propagation of the $D^0 \to K^0_S\pi^+\pi^-$ decay amplitude model uncertainties to those of the *CP* violation parameters. These approaches lead to improvements in the experimental sensitivity and in the robustness of the measurement.

We measure $\sin 2\beta = 0.80 \pm 0.14(\text{stat}) \pm 0.06(\text{syst}) \pm 0.03(\text{model})$, $\cos 2\beta = 0.91 \pm 0.22(\text{stat}) \pm 0.09(\text{syst}) \pm 0.07(\text{model})$, and $\beta = (22.5 \pm 4.4(\text{stat}) \pm 1.2(\text{syst}) \pm 0.6(\text{model}))°$, where the measurement assumes no direct *CP* violation in $B^0 \to D^{(*)}h^0$ decays. The $\sin 2\beta$ value agrees well with more precise measurements using $\bar{b} \to \bar{c}c\bar{s}$ transitions, as well as with our previous measurement combining *BABAR* and Belle data [31]. We exclude the hypothesis of $\beta = 0°$ at a significance of 5.1 standard deviations and report an observation of *CP* violation in $\bar{B}^0 \to D^{(*)}h^0$ decays. We report the world's most precise measurement of the cosine of the *CP*-violating weak phase 2β and obtain the first evidence for $\cos 2\beta > 0$ at the level of 3.7 standard deviations. This measurement directly excludes the trigonometric multifold solution of $\pi/2 - \beta = (68.1 \pm 0.7)°$ without further assumptions and thus resolves the ambiguity in the determination of the apex of the CKM Unitarity Triangle.

Due to the absence of penguin amplitudes, the $B^0 \to D^{(*)}h^0$ decays allow theoretically cleaner access to the *CP*-violating phase 2β than the "gold plated" decay modes mediated by $\bar{b} \to \bar{c}c\bar{s}$ transitions [84]. In measurements of $\sin 2\beta$ and $\cos 2\beta$ using $B^0 \to D^{(*)}h^0$ with $D \to K^0_S\pi^+\pi^-$ decays, the limitations in the achievable precision that originate from the Dalitz plot model uncertainties can be resolved by model-independent approaches that use external experimental knowledge on the relative strong phases of the D meson decays measured at the charm factories [29]. In addition, $\bar{B}^0 \to D^{(*)}_{CP}h^0$ decays with D_{CP} decaying into two-body *CP* eigenstates allow the precise determination of $\sin 2\beta$. Therefore, future measurements of $B^0 \to D^{(*)}h^0$ decays using more data can provide a new and complementary SM reference for 2β.

The combined *BABAR*+Belle approach allows access to an unprecedentedly large data sample totaling more than 1 ab^{-1} recorded at c.m. energies of the $\Upsilon(4S)$ resonance and provides unique experimental precision, in particular, for time-dependent *CP* violation measurements in the neutral B meson system. Our results underline the importance and discovery potential of future heavy flavor physics experiments operated at high instantaneous luminosity such as the B factory experiment Belle II [32], which is expected to collect a data sample of 1 ab^{-1} by the year 2020 and is designed to collect 50 ab^{-1} by the middle of the next decade.

ACKNOWLEDGMENTS

We thank the PEP-II and KEKB groups for the excellent operation of the accelerators. The *BABAR* experiment acknowledges the expertise and dedication of the computing organizations for their support. The collaborating institutions wish to thank SLAC for its support and the kind hospitality extended to them. The Belle experiment wishes to acknowledge the KEK cryogenics group for the efficient operation of the solenoid; and the KEK computer group, the National Institute of Informatics, and the PNNL/EMSL computing group for valuable computing and SINET5 network support. This work was supported by the Ministry of Education, Culture, Sports, Science, and Technology (MEXT) of Japan, the Japan Society for the Promotion of Science (JSPS), and the Tau-Lepton Physics Research Center of Nagoya University; the Australian Research Council; Austrian Science Fund under Grant No. P 26794-N20; the Canadian Natural Sciences and Engineering Research Council; the National Natural Science Foundation of China under Contracts No. 10575109, No. 10775142, No. 10875115, No. 11175187, No. 11475187, No. 11521505 and No. 11575017; the Chinese Academy of Science Center for Excellence in Particle Physics; the Ministry of Education, Youth and Sports of the Czech Republic under Contract No. LTT17020; the French Commissariat à l'Energie Atomique and Institut National de Physique Nucléaire et de Physique des Particules; the German Bundesministerium für Bildung und Forschung, the Carl Zeiss Foundation, the Deutsche Forschungsgemeinschaft, the Excellence Cluster Universe, and the VolkswagenStiftung; the Department of Science and Technology of India; the Istituto Nazionale di Fisica Nucleare of Italy; National Research Foundation (NRF) of Korea Grants No. 2014R1A2A2A01005286, No. 2015R1A2A2A01003280, No. 2015H1A2A1033649, No. 2016R1D1A1B01010135, No. 2016K1A3A7A09005603, and No. 2016R1D1A1B02012900; Radiation Science Research Institute, Foreign Large-Size Research Facility Application Supporting project and the Global Science Experimental Data Hub Center of the Korea Institute of Science and Technology Information; the Foundation for Fundamental Research on Matter of the Netherlands; the Research Council of Norway; the Polish Ministry of

Science and Higher Education and the National Science Center; the Ministry of Education and Science of the Russian Federation and the Russian Foundation for Basic Research; the Slovenian Research Agency; Ikerbasque, Basque Foundation for Science and MINECO (Juan de la Cierva), Spain; the Swiss National Science Foundation; the Ministry of Education and the Ministry of Science and Technology of Taiwan; the Science and Technology Facilities Council of the United Kingdom; the Binational Science Foundation (U.S.-Israel); and the U.S. Department of Energy and the National Science Foundation. Individuals have received support from the Marie Curie EIF (European Union) and the A. P. Sloan Foundation (USA).

[1] M. Gell-Mann and A. Pais, Phys. Rev. **97**, 1387 (1955).
[2] T. D. Lee and C. N. Yang, Phys. Rev. **104**, 254 (1956).
[3] T. D. Lee, Phys. Rep. **9**, 143 (1974).
[4] I. I. Bigi and A. I. Sanda, *CP Violation*, 2nd ed. (Cambridge University Press, Cambridge, England, 2009).
[5] A. D. Sakharov, JETP Lett. **5**, 24 (1967).
[6] M. B. Gavela, P. Hernandez, J. Orloff, and O. Pene, Mod. Phys. Lett. A **09**, 795 (1994).
[7] A. Riotto and M. Trodden, Annu. Rev. Nucl. Part. Sci. **49**, 35 (1999).
[8] N. Cabibbo, Phys. Rev. Lett. **10**, 531 (1963).
[9] M. Kobayashi and T. Maskawa, Prog. Theor. Phys. **49**, 652 (1973).
[10] B. Aubert *et al.* (*BABAR* Collaboration), Phys. Rev. Lett. **87**, 091801 (2001).
[11] K. Abe *et al.* (Belle Collaboration), Phys. Rev. Lett. **87**, 091802 (2001).
[12] B. Aubert *et al.* (*BABAR* Collaboration), Phys. Rev. Lett. **93**, 131801 (2004).
[13] Y. Chao *et al.* (Belle Collaboration), Phys. Rev. Lett. **93**, 191802 (2004).
[14] A. J. Bevan *et al.*, Eur. Phys. J. C **74**, 3026 (2014).
[15] B. Aubert *et al.* (*BABAR* Collaboration), Phys. Rev. D **79**, 072009 (2009).
[16] I. Adachi *et al.* (Belle Collaboration), Phys. Rev. Lett. **108**, 171802 (2012).
[17] Y. Amhis *et al.* (Heavy Flavor Averaging Group), Eur. Phys. J. C **77**, 895 (2017).
[18] B. Aubert *et al.* (*BABAR* Collaboration), Phys. Rev. D **71**, 032005 (2005).
[19] R. Itoh *et al.* (Belle Collaboration), Phys. Rev. Lett. **95**, 091601 (2005).
[20] B. Aubert *et al.* (*BABAR* Collaboration), Phys. Rev. D **74**, 091101 (2006).
[21] J. Dalseno *et al.* (Belle Collaboration), Phys. Rev. D **76**, 072004 (2007).
[22] J. P. Lees *et al.* (*BABAR* Collaboration), Phys. Rev. D **85**, 112010 (2012).
[23] Y. Nakahama *et al.* (Belle Collaboration), Phys. Rev. D **82**, 073011 (2010).
[24] B. Aubert *et al.* (*BABAR* Collaboration), Phys. Rev. D **80**, 112001 (2009).
[25] J. Dalseno *et al.* (Belle Collaboration), Phys. Rev. D **79**, 072004 (2009).
[26] A. Bondar, T. Gershon, and P. Krokovny, Phys. Lett. B **624**, 1 (2005).
[27] P. Krokovny *et al.* (Belle Collaboration), Phys. Rev. Lett. **97**, 081801 (2006).
[28] B. Aubert *et al.* (*BABAR* Collaboration), Phys. Rev. Lett. **99**, 231802 (2007).
[29] V. Vorobyev *et al.* (Belle Collaboration), Phys. Rev. D **94**, 052004 (2016).
[30] A. Bondar and T. Gershon, Phys. Rev. D **70**, 091503 (2004).
[31] A. Abdesselam *et al.* (*BABAR* and Belle Collaborations), Phys. Rev. Lett. **115**, 121604 (2015).
[32] T. Abe, I. Adachi, K. Adamczyk *et al.* (Belle II Collaboration), KEK Report No. 2010-1, High Energy Accelerator Research Organization, Japan, 2010.
[33] I. Adachi *et al.* (*BABAR* and Belle Collaborations), companion Letter, Phys. Rev. Lett. **121**, 261801 (2018).
[34] J. Dorfan *et al.*, PEP-II Conceptual Design Report, SLAC Report No. SLAC-R-418, 1993.
[35] S. Kurokawa and E. Kikutani, Nucl. Instrum. Methods Phys. Res., Sect. A **499**, 1 (2003), and other papers included in this volume; T. Abe *et al.*, Prog. Theor. Exp. Phys. **2013**, 03A001 (2013), and references therein.
[36] A. Abashian *et al.* (Belle Collaboration), Nucl. Instrum. Methods Phys. Res., Sect. A **479**, 117 (2002); also see detector section in J. Brodzicka *et al.*, Prog. Theor. Exp. Phys. **2012**, 4D001 (2012).
[37] B. Aubert *et al.* (*BABAR* Collaboration), Nucl. Instrum. Methods Phys. Res., Sect. A **479**, 1 (2002); **729**, 615 (2013).
[38] J. P. Lees *et al.* (*BABAR* Collaboration), Nucl. Instrum. Methods Phys. Res., Sect. A **726**, 203 (2013).
[39] Z. Natkaniec *et al.* (Belle SVD2 Group), Nucl. Instrum. Methods Phys. Res., Sect. A **560**, 1 (2006).
[40] D. J. Lange, Nucl. Instrum. Methods Phys. Res., Sect. A **462**, 152 (2001).
[41] T. Sjöstrand, Comput. Phys. Commun. **82**, 74 (1994).
[42] P. Golonka and Z. Was, Eur. Phys. J. C **45**, 97 (2006).
[43] S. Agostinelli *et al.*, Nucl. Instrum. Methods Phys. Res., Sect. A **506**, 250 (2003).
[44] R. Brun *et al.*, GEANT 3.21, CERN Report No. DD/EE/84-1, 1984.
[45] C. Patrignani *et al.* (Particle Data Group), Chin. Phys. C **40**, 100001 (2016).
[46] K. F. Chen *et al.* (Belle Collaboration), Phys. Rev. D **72**, 012004 (2005).
[47] N. L. Johnson, Trab. Estadist. **5**, 283 (1954).
[48] J. E. Gaiser *et al.* (Crystal Ball Collaboration), Phys. Rev. D **34**, 711 (1986).

[49] See the review on Dalitz plot analysis formalism in J. Beringer *et al.* (Particle Data Group), Phys. Rev. D **86**, 010001 (2012), and references therein.

[50] S. U. Chung, J. Brose, R. Hackmann, E. Klempt, S. Spanier, and C. Strassburger, Ann. Phys. (N.Y.) **507**, 404 (1995).

[51] D. Aston *et al.* (LASS Collaboration), Nucl. Phys. **B296**, 493 (1988).

[52] F. von Hippel and C. Quigg, Phys. Rev. D **5**, 624 (1972).

[53] C. Zemach, Phys. Rev. **133**, B1201 (1964); **140**, B97 (1965).

[54] P. del Amo Sanchez *et al.* (*BABAR* Collaboration), Phys. Rev. Lett. **105**, 081803 (2010).

[55] T. Peng *et al.* (Belle Collaboration), Phys. Rev. D **89**, 091103 (2014).

[56] The CKM angle γ is also referred to as ϕ_3 in the literature.

[57] B. Aubert *et al.* (*BABAR* Collaboration), Phys. Rev. D **78**, 034023 (2008).

[58] R. Aaij *et al.* (LHCb Collaboration), Nucl. Phys. **B888**, 169 (2014).

[59] I. J. R. Aitchison, Nucl. Phys. **A189**, 417 (1972).

[60] V. V. Anisovich and A. V. Sarantsev, Eur. Phys. J. A **16**, 229 (2003); and private communication with the authors from [57].

[61] S. L. Adler, Phys. Rev. **137**, B1022 (1965).

[62] B. Aubert *et al.* (*BABAR* Collaboration), Phys. Rev. D **79**, 112001 (2009).

[63] L. Dagum and R. Menon, IEEE Comput. Sci. Eng. **5**, 46 (1998).

[64] OpenMP Architecture Review Board, OpenMP Application Program Interface Version 4.0, http://www.openmp.org/mp-documents/OpenMP4.0.0.pdf.

[65] A. Poluektov *et al.* (Belle Collaboration), Phys. Rev. D **81**, 112002 (2010).

[66] T. Aaltonen *et al.* (CDF Collaboration), Phys. Rev. D **86**, 032007 (2012).

[67] P. del Amo Sanchez *et al.* (*BABAR* Collaboration), Phys. Rev. D **83**, 052001 (2011).

[68] G. J. Gounaris and J. J. Sakurai, Phys. Rev. Lett. **21**, 244 (1968).

[69] A. Poluektov *et al.* (Belle Collaboration), Phys. Rev. D **70**, 072003 (2004).

[70] J. Libby *et al.* (CLEO Collaboration), Phys. Rev. D **82**, 112006 (2010).

[71] B. Aubert *et al.* (*BABAR* Collaboration), Phys. Rev. Lett. **99**, 081801 (2007).

[72] M. Nakao *et al.* (Belle Collaboration), Phys. Rev. D **69**, 112001 (2004).

[73] M. Feindt and U. Kerzel, Nucl. Instrum. Methods Phys. Res., Sect. A **559**, 190 (2006).

[74] The Fox-Wolfram moments were introduced in G. C. Fox and S. Wolfram, Phys. Rev. Lett. **41**, 1581 (1978); The modified Fox-Wolfram moments used in this article are described in S. H. Lee *et al.* (Belle Collaboration), Phys. Rev. Lett. **91**, 261801 (2003).

[75] Y. M. Goh *et al.* (Belle Collaboration), Phys. Rev. D **91**, 071101 (2015).

[76] H. Ikeda *et al.* (Belle Collaboration), Nucl. Instrum. Methods Phys. Res., Sect. A **441**, 401 (2000).

[77] H. Albrecht *et al.* (ARGUS Collaboration), Phys. Lett. B **241**, 278 (1990).

[78] B. Aubert *et al.* (*BABAR* Collaboration), Phys. Rev. D **66**, 032003 (2002).

[79] H. Tajima *et al.*, Nucl. Instrum. Methods Phys. Res., Sect. A **533**, 370 (2004).

[80] H. Kakuno *et al.*, Nucl. Instrum. Methods Phys. Res., Sect. A **533**, 516 (2004).

[81] M. Röhrken, *Time-Dependent CP Violation Measurements* (Springer, Berlin, 2014), pp. 71–106, https://www.springer.com/gp/book/9783319007250.

[82] M. Pivk and F. R. Le Diberder, Nucl. Instrum. Methods Phys. Res., Sect. A **555**, 356 (2005).

[83] A. Einstein, B. Podolsky, and N. Rosen, Phys. Rev. **47**, 777 (1935).

[84] R. Fleischer, Phys. Lett. B **562**, 234 (2003); Nucl. Phys. **B659**, 321 (2003).